RESEARCH ARTICLE | APRIL 04 2023

Computational and experimental studies of wave–structure interaction: Wave attenuation by a floating breakwater

N. N. Peng ; W. K. Lau ; O. W. H. Wai; K. W. Chow

Physics of Fluids 35, 045112 (2023)
https://doi.org/10.1063/5.0142991

Physics of Fluids ARTICLE scitation.org/journal/phf

Computational and experimental studies of wave–structure interaction: Wave attenuation by a floating breakwater

Cite as: Phys. Fluids **35**, 045112 (2023); doi: 10.1063/5.0142991
Submitted: 19 January 2023 · Accepted: 14 March 2023 ·
Published Online: 4 April 2023

N. N. Peng,[1,a)] W. K. Lau,[1] O. W. H. Wai,[2] and K. W. Chow[1,b)]

AFFILIATIONS

[1]Department of Mechanical Engineering, University of Hong Kong, Pokfulam, Hong Kong
[2]Department of Civil and Environmental Engineering, Hong Kong Polytechnic University, Hung Hom, Hong Kong

[a)]Author to whom correspondence should be addressed: peng2nn@connect.hku.hk
[b)]Electronic mail: kwchow@hku.hk

ABSTRACT

Interactions between surface gravity waves and a floating rigid body are complex, as waves may reflect from, break on, and be transmitted behind the body. Studies of these phenomena are critically important in improving the safety and functional efficiency of offshore structures. Here, the wave attenuation performance and motions of a type of floating breakwater (FB) are studied through numerical and experimental approaches. A numerical wave tank (NWT) is developed based on the software OpenFOAM and properties of wave channel from a laboratory. In the NWT, the air–water interface is captured by the volume of fluid method. The motions of FB are tracked by the six degrees of freedom model. A mooring system model is developed to simulate the constraints of the FB. Large eddy simulation turbulence modeling is implemented for the wave breaking processes. A model FB with a scale of 1:20 is tested in both the experimental and numerical wave channel. Wave heights at the back/front of the FB and the constraint forces of the mooring wires are measured. The numerical models are validated by comparing the results with experimental measurements. The variations of transmission/reflection coefficients, energy dissipation rate, and maximum mooring force are calculated. Changes of the response amplitude operators with the ratio of FB width to wavelength (B/L_w) and wave steepness are analyzed. The wave transmission coefficient will drop below 0.8 if the value of B/L_w is larger than 0.3, but will go over 0.95 if B/L_w is less than 0.1. Wave steepness has a large influence on FB motions and the mooring system. The effect of Stokes drift is observed by the shift of position of the FB.

I. INTRODUCTION

Floating breakwater (FB) constitutes a common and relatively cost-effective method for the protection of small harbors, marinas, and the control of shoreline erosion. It is especially useful for situations when mounted breakwater encounters difficulties due to large water depth or complex seafloor. Historically, the first FB was probably deployed at Plymouth Port in England in 1811. Dai *et al.*[1] and McCartney and ASCE[2] delineated FBs depending on their geometry and fundamental features. Alternatively, Sawaragi[3] classified FBs into three groups (reflection type, reflection/wave breaking type, and friction type), according to the wave attenuation mechanisms. Both wave breaking and friction lead to wave dissipation.

The main function of the floating breakwater is to attenuate the incident wave height by reflection or dissipation. Recently, intensive attention is focused on new FBs combining these two mechanisms, especially pontoons with accessories that can increase wave dissipation. Peña *et al.*[4] evaluated the performance of four different designs of pontoon type FB and found that the width of the pontoons will constitute one key design parameter. Ji *et al.*[5–7] studied experimentally and numerically the hydrodynamic behavior of dual cylindrical pontoon type FBs attached to one or more rows of plane net. Christensen *et al.*[8] investigated the effect of two different damping mechanisms, wave radiation and viscous damping, on a rectangular pontoon FB by adding wing plates and porous media to the sides. Zhan *et al.*[9] presented a numerical analysis of the nonlinear interaction between inverse T-type free surface breakwater and regular/irregular waves using a zonal hybrid RANS (Reynolds-averaged Navier–Stokes)/laminar method.

There is another type of plastic FBs commonly used in small marinas and beaches against short waves and wakes. Wang and Sun[10] introduced a novel configuration of FB fabricated with large numbers

of diamond-shaped blocks and described its performance for wave attenuation. A porous FB can achieve wave reduction performance by increased wave breaking and lower mooring force.[6,8,10] FBs with a cross section extended by wings or similar geometric protrusion can reduce the motion of FB significantly.[8,9] In the present work, an assembly of FBs consisting of small plastic modules with a trapezoid cross section will be studied numerically and experimentally [Fig. 1(a)]. These products are manufactured by the WhisprWave Company [Fig. 1(b)]. The FB is made of HDPE (high-density polyethylene) modules and can also be linked together with different configurations to achieve the wave reduction function.

Interactions between surface gravity waves and maritime structures are complex. Waves may be reflected by and/or transmitted behind the FB. Moreover, diffraction, breaking, and overtopping of waves will occur, rendering the analysis exceedingly difficult. Analytical solutions were deduced for specific scenarios with simple configurations or related issues, e.g., wave attenuation by porous viscoelastic material.[11–13] Early works on the practical applications of FBs have actually been carried out through experimental approaches. Wave gauges, force sensors, and accelerometers are used for measurements of wave profile, mooring forces, and motions of objects, respectively.[6,8,14] With state-of-the-art measurement techniques of fluid flow, such as particle imaging (or tracking) velocimetry (PIV or PTV), the velocity field can be obtained with sufficient resolution and accuracy to study the wave–structure interactions.[15–17] Furthermore, high-speed cameras coupled with advanced machine learning algorithms had been implemented to investigate the turbulent flow and breaking waves generated by wave–structure interactions.[18] In the present work, the complex geometry makes tracking the motions of the FB experimentally an extremely difficult task.

Several numerical methods had been developed recently for wave–structure interactions, due to fast-growing computer technology and the development of novel computational physics.[19–22] Smoothed particle hydrodynamics (SPH) is increasingly used to model multiphase flow, as it is mesh-free and is capable to create a free surface directly.[23–25] The finite volume method (FVM)[26,27] traces the time-varying free surface by algorithms such as the Level Set method (LSM)[28] or the volume of fluid (VOF) method.[29] As polyhedral mesh will exist in the body-fit mesh around the FB, VOF will be employed with special interface sharpening technology in this work. For fluid and structure interaction (FSI) situations, the motions of a rigid body, e.g., FB, are simulated by the six degrees of freedom (6DoF) model.[30] Turbulence will make a significant contribution to wave dissipation. The large eddy simulation (LES) method is utilized to achieve a balance between computational accuracy and constraints on resource. Indeed, LES and VOF methods have been extensively used for studying wave–structure interactions and energy dissipation during wave-breaking,[31–34] especially in the presence of air bubble entrainment.[35–37] In comparison with laboratory measurements, numerical simulations serve as a flexible and cost-effective alternative, offering access to all variables for detailed analysis.

In our previous work,[38] a three-dimensional (3D) numerical wave tank (NWT) for wave propagation and breaking is developed based on OpenFOAM. Computationally significant factors like grid size, relaxation weight, and time step are investigated to find the optimal parameters of the numerical models for various wave propagation regimes. The accuracy and performance of the NWT in terms of reflection coefficient, wave damping, and phase distortion rates are elucidated. The capacity to simulate wave breaking process is confirmed by comparing the numerical results with experimental data. In the present study, the developed NWT model is utilized and improved to study wave–floating structure interactions. The performance and motions of a FB consisting of plastic modules held by wires to the seabed are studied by both numerical and experimental approaches. Wave properties and mooring forces are measured in a laboratory. Concurrently, a numerical wave tank mimicking the physical device is developed based on the finite volume method (FVM). The sequence of presentation can now be explained. A detailed description of the design of the FB is given (Sec. II). The theoretical formulation and numerical schemes are elucidated (Sec. III). The experimental setup in the laboratory is described (Sec. IV). Analysis of the experimental and numerical results is performed (Sec. V). Finally, conclusions are drawn (Sec. VI).

II. FLOATING BREAKWATER

The physical prototype of the FB consists of a sequence of identical modules. Each module is a closed-shell filled with foam [Fig. 2(a)], connected into a three-layer structure component by tying wire and other accessories [Figs. 2(b) and 2(c)]. A 10-m-long FB segment includes 152 modules, 78 of which are in the bottom layer.

Experimentally, a model with a scale factor of 1:20 is employed. The present FB consists of a regular arrangement of base units [Fig. 2(c)] with prescribed linear dimensions [Fig. 2(d)]. To reduce the effects of wave diffraction, the laboratory-scaled model consists of 25 base units and is 1 m long. To achieve efficient usage of computational resources, the floating breakwater is simplified as one base unit with special treatment of boundary conditions.

(a) (b)

FIG. 1. (a) Physical model of the FB, WhisrWave, (b) an illustrative case implemented near a seawall in Hong Kong (Courtesy of the Drainage Services Department, Hong Kong Special Administrative Government).

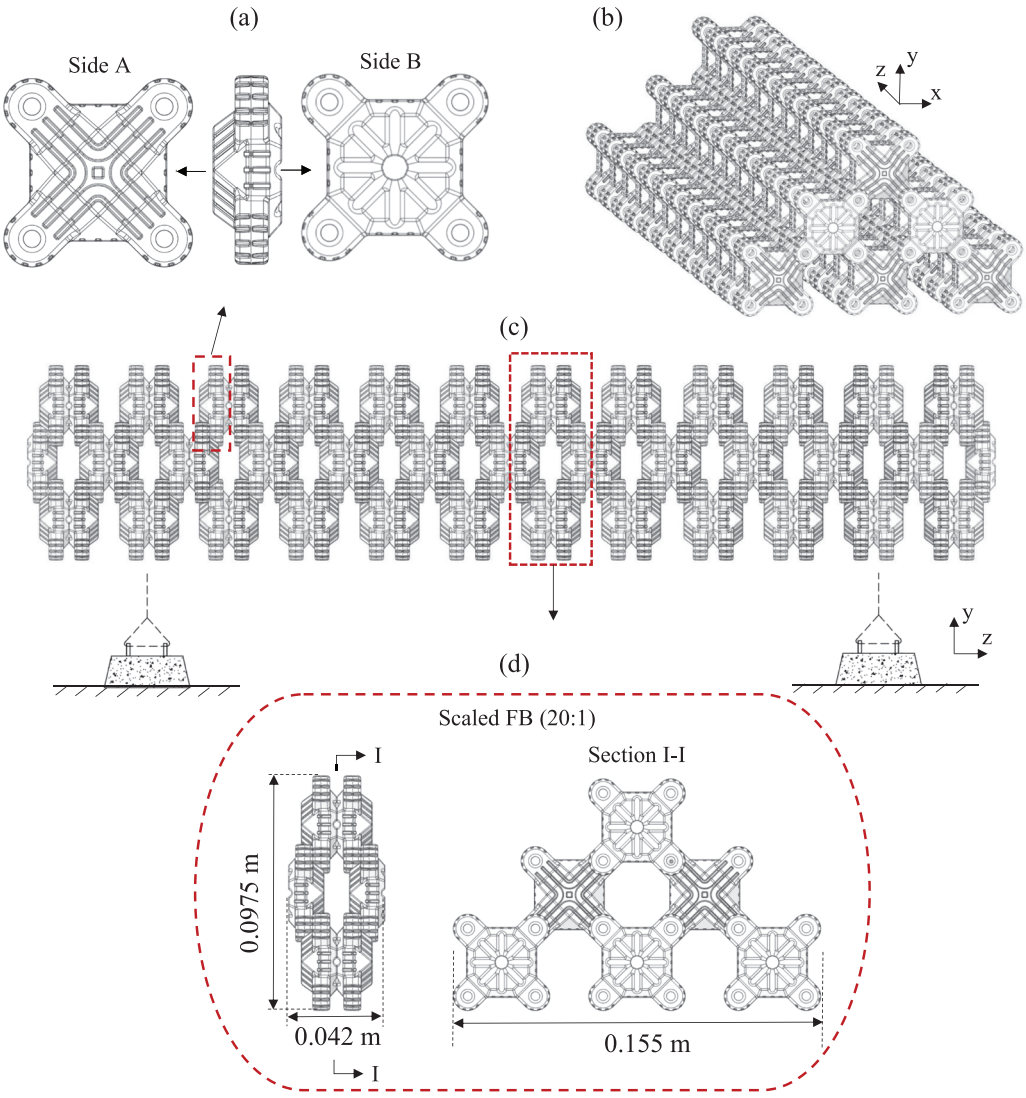

FIG. 2. Schematic diagram of the geometry and installation of the FB: (a) detailed structure of a module, (b) side view and (c) front view of FB, and (d) detailed structure of a base unit.

III. NUMERICAL MODELING

A. Computational domain and mesh

A three-dimensional model of the wave channel and FB is developed (Fig. 3). Simulations with free surface and dynamical meshes are generally computationally expensive. The numerical FB model is simplified as one base unit [Fig. 3(d)], and the surface features of modules are ignored [Fig. 3(b)]. The computational domain is reduced in the z axis direction as a simplification of the FB model. For the dimensions of the numerical wave tank (NWT), the length in the x-direction is 12 times the wavelength of the tested wave. Gravity acts in the negative y direction, and the y-dimension of the domain is 1.2 m. The precise dimension in the z-direction will depend on the specific scenarios tested. For one base unit of FB, the NWT adopted is 0.042 m wide in the z-direction. To avoid wave reflection at the inlet and outlet boundaries, two relaxation zones are deployed.

The detailed setup of the NWT for the types of waves tested, the configuration of the relaxation zone, as well as the spatial and temporal discretization resolution, are described in our previous work.[38] The relaxation zone method is implemented to account for the generation and absorption of waves at the inlet/outlet boundaries. A high spatial resolution is needed at the interface. Accordingly, a finer grid is imposed near the interface (in the region from $z = 0.59$ to $z = 0.61$), with a grid size $\Delta z = 0.0001$ m. To minimize numerical errors in the wave propagation process. The appropriate grid size and time step should be determined by the wavelength and period.[39,40] LES simulations require a grid that can resolve low-frequency eddies containing 80% or more of the energy spectrum.

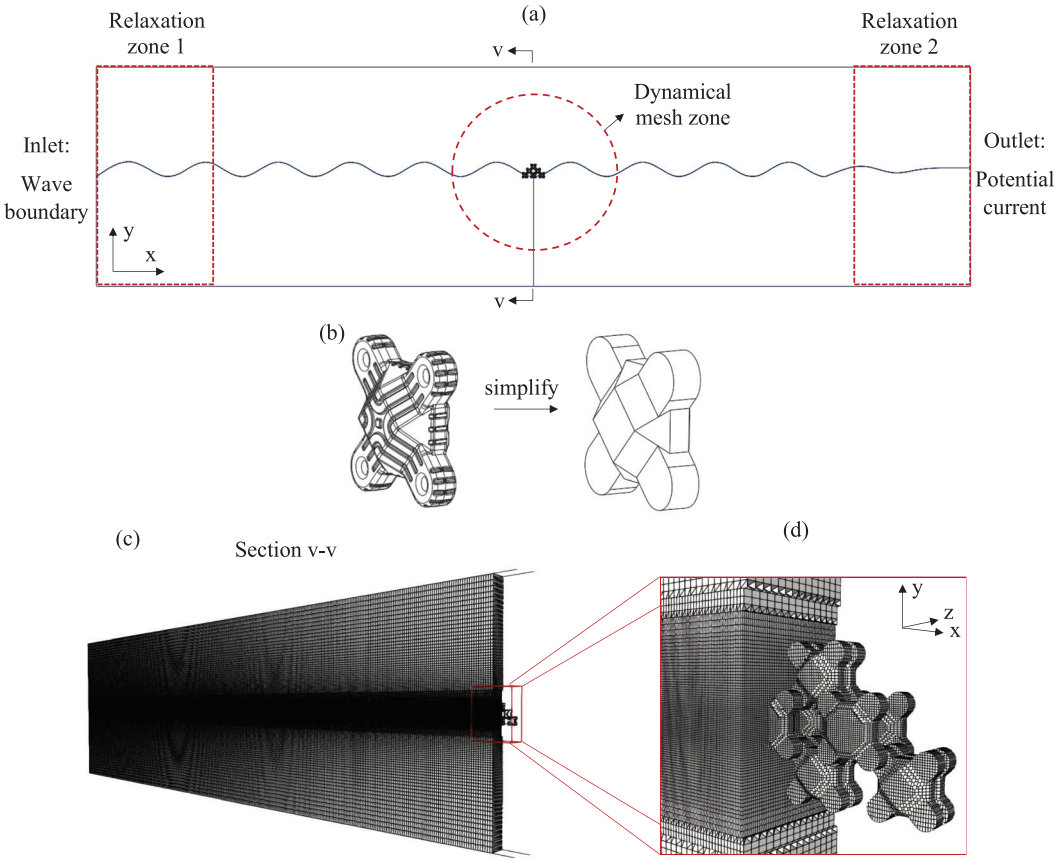

FIG. 3. Diagrams of computational tests: (a) overall dimensions and setup of NWT, (b) simplification of FB modules, (c) 3D mesh of the left half of NWT, and (d) detailed view of the surface mesh of the FB boundaries.

The size of the present grid in the directions of gravity and wave propagation directions are smaller than $H_w/20$, and $L_w/80$, respectively, where H_w is wave height and L_w is the wavelength. The grid size in the z-direction is 0.006 m. Interconnections among the grid ratio, wavelength, maximum Courant number, and wave period are discussed in a previous study Peng and Chow[38] (Fig. 4). The performance of relaxation zone methods has been assessed in many studies.[41,42] To reduce the reflection coefficient at the outlet boundary to be 1% or less, the length of the relaxation zone is set to be two to three wavelengths, which is longer than those adopted in relevant studies.

In transient simulations of wave–FB interactions, the position of FB is changing with time. The computational domain, which is surrounded by walls of the wave tank and surfaces of the FB, thus needs to be updated at every time step based on the new position of the rigid body. The *snappyHexMesh* utility provided by OpenFOAM has been used to generate a layer-adapted mesh. The grid size in a region surrounding the FB is further refined to 1 mm to ensure the mesh quality and the capacity to resolve wave-breaking phenomenon in this area [Fig. 3(d)]. The dynamic mesh solver then updates the mesh configuration according to the position of the rigid body. The detailed dynamical mesh scheme will be presented in Sec. III B 5.

B. Mathematical models

Wave–FB interaction is a multiphase-flow problem involving air, water, and fluid–rigid-body interaction issues. The numerical model will invoke these schemes and elements:

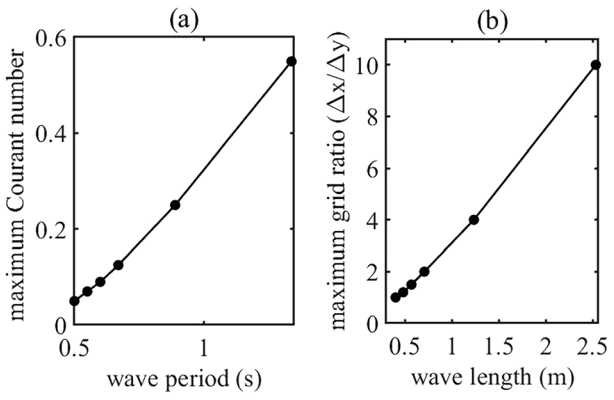

FIG. 4. Relation among (a) the maximum Courant number and wave period, (b) grid ratio and wavelength.

- the volume of fluid (VOF) scheme for capturing the moving free surface,
- boundary condition for generating the necessary incident Stokes waves,
- the relaxation zone model for minimizing the effect of reflecting waves,
- the six degrees of freedom (6DoF) method for predicting the motion of the FB,
- a mooring system model for simulating the restraints on the movements of the FB.

1. Free surface flow modeling

Water and air are assumed to be incompressible, isothermal, and immiscible fluids. The VOF method is used for simulating this multiphase flow. Both fluids are described by a single set of governing equations. Both fluids are described by a single set of governing equations, the continuity and 3D Navier–Stokes equations [Eq. (1)],[43]

$$\frac{\partial \rho}{\partial t} + \nabla \cdot (\rho \mathbf{u}) = 0, \tag{1a}$$

$$\frac{\partial (\rho \mathbf{u})}{\partial t} + \nabla \cdot (\rho \mathbf{u}\mathbf{u}) - \nabla \cdot \tau = -\nabla p + \rho g + f_\sigma + f_{FB}. \tag{1b}$$

Velocity u, density ρ, and pressure p are the fluid properties of the air–water mixture, f_σ is the surface tension, and f_{FB} is the counterforce from the FB. In interFoam-based solvers provided by OpenFOAM, the pressure p is more beneficially represented by an alternative pressure defined by $p_{rgh} = p - \rho g h$, where h is the relative distance between the local cell and a reference level in the direction of gravity.[44] Surface tension is a special property of liquid due to the cohesive nature of the molecules which usually plays a significant role for small scale (a few centimeters or smaller) free and forced surface waves. In particular, surface tension effects should be incorporated for

- strongly nonlinear waves with large interface deformation,[45] and
- breaking waves with a length scale shorter than 4 m and amplitude smaller than 0.11 m (Ref. 46).

A continuum surface force (CSF) model[47] is then implemented to replace the surface tension force with a volume force, f_σ, due to surface tension on fluid elements lying within a finite thickness transition region. The surface tension force could be denoted as a function of the surface tension, σ, and the surface curvature, κ,

$$f_\sigma = \sigma \kappa \nabla \alpha, \quad \kappa = \nabla \cdot \left(\frac{\nabla \alpha}{|\nabla \alpha|} \right).$$

The surface tension of the air–water surface at ambient temperature (20 °C) is 72.9 mN/m. The surface tension constant σ is set to be 0.07.

The interface between air and water is governed by the phase fraction transport equation [Eq. (2)] in the VOF method,[29]

$$\frac{\partial \alpha}{\partial t} + \mathbf{u} \cdot \nabla \alpha = 0. \tag{1c}$$

In the phase fraction transport equation, the volume fraction of fluid (water), α, is introduced to represent the mixture of fluids in each computational cell. When α is equal to 0 or 1, the computational cell is filled completely with air or water, respectively. Otherwise, the cell is at the interface. Based on the local value of α, from 0 to 1, the properties of the mixture (denoted as ϕ), including density, velocity, and dynamic viscosity, can be expressed through phase fraction α,

$$\phi = \alpha \phi_{water} + (1 - \alpha)\phi_{air}.$$

Due to the discontinuity nature at the interface, special interpolation schemes are required to capture the sharp interfaces between the phases and avoid interfacial oscillations during a simulation.[48,49] In the present work, a hybrid interpolation scheme provided in the OpenFOAM library, which is based on piecewise-linear interface calculation (PLIC) and interface compression is applied in the phase fraction equation.[50–52] PLIC reconstructs an interface of second-order accuracy by surface-cut, which splits each cell to match the volume fraction of the phase in that cell. For cells with multiple interfaces or where the interface is not fully resolved, the interpolation reverts to an alternative scheme, the standard interface compression which is based on counter-gradient transport. An artificial advective term including a compression factor θ_c is then added to the transport equation of phase fraction,

$$\frac{\partial \alpha}{\partial t} + \mathbf{u} \cdot \nabla \alpha + \nabla \cdot \left(\alpha(1 - \alpha)\theta_c |\mathbf{u}| \frac{\nabla \alpha}{|\nabla \alpha|} \right) = 0. \tag{2}$$

A compression factor θ_c being 0 or 1 corresponds to no compression effect or conservative compression, respectively. A value larger than unity represents an enhanced compression scenario.

2. Six degrees of freedom model (6DoF)

The FB is assumed to be a rigid body moving without deformation during the interactions with wave flow. This motion of a rigid body is calculated based on the fluid forces and other external forces acting on the FB. In turn, the motion solver of FB provides feedback to the fluid simulation. The six degrees of freedom model (6DoF)[30,53] is utilized to predict the motions of FB. This 6DoF dynamical model allows the FB to execute three-dimensional motions under the influence of fluid flow and external constraints like mooring. Forces and moments acting on the FB are expressed as follows:

$$\sum \mathbf{F} = \mathbf{f}_{moor} + \mathbf{f}_{buoy} + \mathbf{G},$$

$$\sum \mathbf{M} = \sum (\mathbf{r}_i - \mathbf{r}_c) \times \mathbf{f}_i,$$

where $\mathbf{f}_{buoy}$ is the net force from the fluid, $\mathbf{f}_{moor}$ is the external force from the mooring system, $\mathbf{G}$ is the weight of the FB, $\mathbf{f}_i$ denotes the forces that can contribute to the moment, $\mathbf{r}_i$ is the coordinate of the corresponding action point, and $\mathbf{r}_c$ is the coordinate of the center of rotation.

The position and velocities of FB can be regarded as boundary conditions for the main fluid solver, while the 6DoF solver will calculate the linear and angular accelerations of FB through the conservation laws of linear and angular momentum,

$$\sum \mathbf{F}_i = \frac{d\mathbf{L}}{dt} = \frac{d(m\mathbf{u}_I)}{dt},$$

$$\sum \mathbf{M}_i = \frac{d\mathbf{H}}{dt} = \frac{d(\mathbf{I}_I \cdot \boldsymbol{\omega}_I)}{dt}.$$

$\mathbf{L}$ and $\mathbf{H}$ are the linear and angular momentum, respectively, and $\boldsymbol{\omega}_I$, $\mathbf{u}_I$, and $\mathbf{I}_I$ are the rotation vector, velocity vector, and moment of

inertia matrix of the rigid body expressed in the inertial reference frame. Generally, the direction of the angular momentum is not in the direction of the rotation vector. In an inertial frame (fixed to the wave tank) that is stationary, the updates of moments of inertia, $\mathbf{I}_I$, are complex due to the rotation and irregular geometry of FB. To avoid this difficulty, the motions of the rigid body could be formulated in an axis system fixed to the rigid body, which is a body-fixed frame. While in the body-fixed frame, which is not an inertial frame, Newton's and Euler's laws cannot be applied directly. By converting the derivative d/dt from the inertial axis to the fixed-body axis, the governing equations of the rigid body are expressed as follows:

$$\sum \mathbf{F}_i = \frac{d(m\mathbf{u})}{dt} + \boldsymbol{\omega} \times (m\mathbf{u}),$$
$$\sum \mathbf{M}_i = \frac{d(\mathbf{I} \cdot \boldsymbol{\omega})}{dt} + \boldsymbol{\omega} \times (\mathbf{I} \cdot \boldsymbol{\omega}).$$

The quantities $\mathbf{u} = (u, v, w)$, $\boldsymbol{\omega} = (\omega_1, \omega_2, \omega_3)$ are the velocity vector, rotation vector about mass center, and $\mathbf{I}$ is the moment of inertia of the rigid body expressed in the body-fixed frame. In OpenFOAM, the angular momentum of the rigid body is stored in the body-fixed frame. The body-fixed axes are chosen to align with the principal axes of the FB, such that the cross product of inertia $\mathbf{I}_{x_i x_j} (i \neq j)$ is zero and the inertia tensor is in principal component form. The conservation of angular momentum is then expressed in terms of moments of inertia about the principal axes,

$$M_x = I_{xx}\alpha_1 + \omega_3\omega_2(I_{zz} - I_{yy}),$$
$$M_y = I_{yy}\alpha_2 + \omega_1\omega_3(I_{xx} - I_{zz}),$$
$$M_z = I_{zz}\alpha_3 + \omega_2\omega_1(I_{yy} - I_{xx}),$$
$$F_x = m(\alpha_1 + \omega_2 w - \omega_3 v),$$
$$F_y = m(\alpha_2 + \omega_3 u - \omega_1 w),$$
$$F_z = m(\alpha_3 + \omega_1 v - \omega_2 u).$$

These expressions constitute the rotational and translational equations of the FB. Since the axes are fixed to the body, it is easy to follow the changes in axis location as the body rotates. Three solvers of the equation set are provided in OpenFOAM, including Newmark, symplectic, and CrankNicolson.

3. Mooring system model

The FB is held to the bottom of the wave channel by mooring wires. In the laboratory study, the mooring line is modeled by a nylon wire. The maximum mooring force measured by load cells is smaller than 6 N. With reference to the tension elongation curves from the previous works[54,55] and the data of the laboratory tests, a nonlinear spring model is developed for the physical mooring system. In the NWT, the mooring wire is represented as a hybrid model of a nonlinear spring and a no-tension joint, depending on the distance L between the FB and the anchor point. The rest length of the mooring wire is denoted by L_{rest}. When the distance L is larger than L_{rest}, the FB is held in place by a wire under tension. Otherwise, the FB is considered as being freely suspended in water. Theoretically, the tension force f_{moor} is calculated as

$$f_{moor} = \begin{cases} k(L - L_{rest}) & \text{if } L \geqslant L_{rest}, \\ 0 & \text{if } L < L_{rest}, \end{cases}$$

where k is the spring stiffness, which measures the resistance offered by an elastic body to deformation. In this mooring wire model, the stiffness measured by a cubic function (Fig. 5),

$$k = 5 + k_c\left(\frac{\Delta l}{\Delta l_{max}}\right), \quad k_c = 150,$$

where k_c is the maximum axial stiffness, Δl is the extension of rope, and Δl_{max} (the maximum extension of rope before breaking) is set to be 5% of the rest length of the mooring line. The unit of stiffness entry k in OpenFOAM is N/m. This nonlinear mooring system model is validated by experimental results in Sec. V B.

4. Wave generation and absorption

Proper boundary conditions (BCs) should be implemented at the inlet and outlet of the NWT for generating and absorbing waves. The relaxation zone method is adopted at both the inlet and outlet boundaries to avoid wave reflection. A Dirichlet-type wave BC[41,42] at the inlet is employed for the velocities, phase fraction, and pressure from a typical finite amplitude wave train, e.g., the fifth-order Stokes wave.[56] In the relaxation zone at the inlet, all fluid variables are gradually made to change from analytical values specified by the Stokes wave BC to computational values. The BC at the outlet for all variables is the fixed value type. In the relaxation zone of the outlet, all fluid variables are also gradually varied from the computational values to fixed values specified by the outlet BCs. More precisely, velocities are smoothly reduced to zero, the free surface is brought to the still water level, and the pressure is relaxed to the hydrostatic value.

The relaxation zone technique is based on a linear combination between the computed and target solution of the fluid variable. The explicit approach in the relaxation zones is given as follows:

$$\phi = \chi_R \phi_{computed} + (1 - \chi_R)\phi_{target}, \quad \chi_R = 1 - \frac{e^{\sigma} - 1}{e - 1}, \quad \sigma = \hat{x}^{3.5},$$

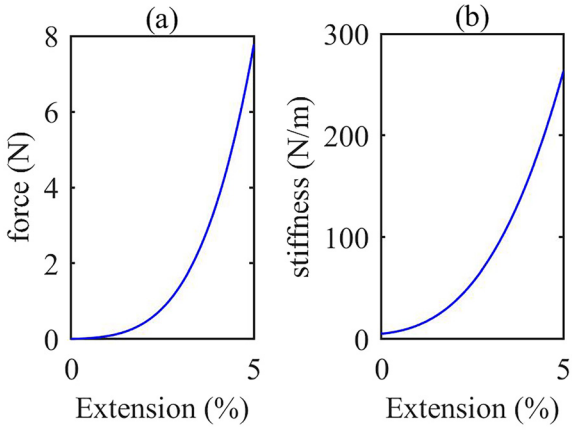

FIG. 5. Mooring system model: (a) mooring force and (b) stiffness coefficient.

where χ_R the relaxation weight is a function of a local coordinate system, $\hat{x}$, in the relaxation zone. Here, the weight is presented as an exponential function with a coefficient being set to 3.5 as suggested by Fuhrman *et al.*[57] The relaxation weight will be used to update the values of the fluid parameters after each time step. If the time step is very small, repeated multiplications by the relaxation weight in a short time interval then will result in a sharp decay of wave variables in the relaxation zones. To avoid this problem, the relaxation weight will be corrected based on the local Courant number, *Co*, and the maximum Courant number, Co_{max}, as follows:[58]

$$\chi_R = \chi_R^{Co/Co_{max}}.$$

5. Dynamic mesh scheme

The computational fluid domain often changes because of the deformation or motions of one or more boundaries. Dynamic mesh models, including, but not limited to, mesh morphing, slide mesh, and overset mesh, allow the mesh varying with the computational domain. Mesh morphing technology accommodates the motion of boundaries by simply moving the grid points without changes in topology and the number of nodes. In comparison with other dynamic mesh methods, it introduces no further discretization error and is easier to implement. However, for large deformation cases, this scheme may lead to mesh quality issues and difficulties in convergence.

The extent of the movement of the FB is relatively small in comparison with the dimensions of the whole NWT. Consequently, a partial mesh morphing scheme, instead of a re-meshing of the entire computational domain, is utilized for reducing the computational cost. Only the grid in a specific region, namely, the dynamic mesh zone [Fig. 3(a)], is morphed to accommodate the position changes of the FB with time. The dynamic mesh area is defined by the distance from the FB, a region between two concentric spheres. The radii are specified, respectively, through two parameters, innerDistance, and outerDistance. The center point aligns with the mass center of the FB.[44] The motions of the boundary are divided into two classes, prescribed and solution-dependent boundary motion. For the latter, additional equations of motion, e.g., 6DoF equations, should be solved for the displacement of points of the surface grid on the moving boundary, r_d. The point displacement then is added to the position of the points at the previous time step, r^n, to obtain the location of the new points, r^{n+1}, (Ref. 59)

$$r^{n+1} = r^n + r_d.$$

The 6DoF solver will resolve the motion and position of the FB based on hydrodynamic forces and external restraints assigned to the FB. The points of the mesh in the dynamic mesh region will move according to the previously solved displacements to adjust to the new position of the FB (Fig. 6).

A high-quality mesh smoothing method, e.g., Laplacian smoothing, is needed for a smooth transition from the displacement of the moving boundaries toward zero displacement at the outer boundaries. In OpenFOAM, several solvers are provided to treat the mesh motion equation, e.g., "displacementLaplacian" and "displacementSBRStress," which handle the elliptic Laplace equation and the solid body rotation (SBR) stress equation, respectively, for the displacement.[44] Typically, the FVM provides the solution in cell centers, but a description of the motion is required on grid points. Hence, a cell-center mesh motion equation and interpolation schemes are implemented. In the present work, the Laplacian smoothing method is utilized. The dynamic mesh area is considered as a linear elastic body, and the cell center displacement, c_d, is governed by the Laplace equation with variable diffusivity,

$$\nabla \cdot (\gamma \nabla c_d) = 0, \quad \gamma = \frac{1}{l}.$$

The variable diffusivity, γ, controls the diffusion of the mesh motion through this area. Efficient diffusivity choices are functions of cell distance to the nearest moving boundary of FB, *l*, and the default choice is the inverse of the distance. Once the cell center displacement is obtained, the spherical linear interpolation (SLERP) of displacement and rotation is used by default to define the point displacement of mesh in a dynamic region, r_d, based on the distance of each grid cell from the moving surface of Fig. 7(c).

6. Turbulence model

Large eddy simulation (LES) is utilized for providing information about turbulent flows. LES calculates the large, energy-carrying eddies explicitly, and quantifies the small eddies through a sub-grid scale (SGS) turbulence model. All variables of the flow field, including the velocity $\bar{\mathbf{u}}$ and the pressure $\bar{p}$, are treated with a filter of dimension of the mesh size, except for the SGS stress tensor τ_{sgs}, which is resolved by a local one-equation eddy viscosity SGS model,[60]

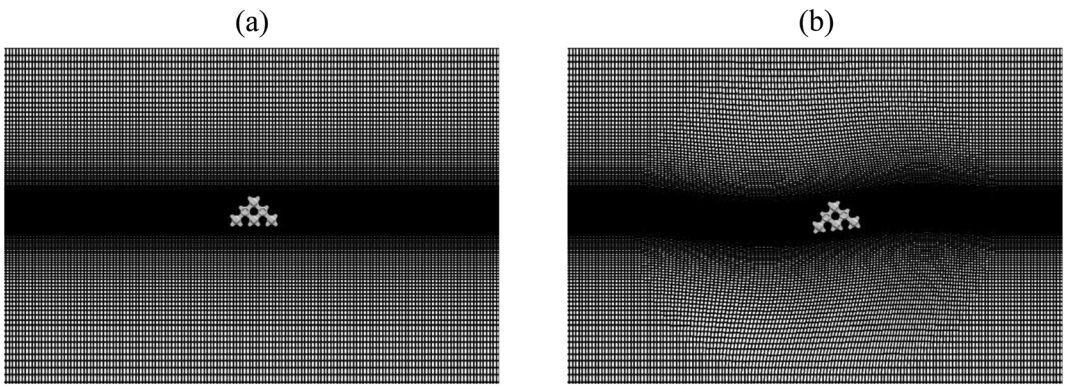

FIG. 6. Mesh morphing: (a) t/T = 0 and (b) t/T = 0.5.

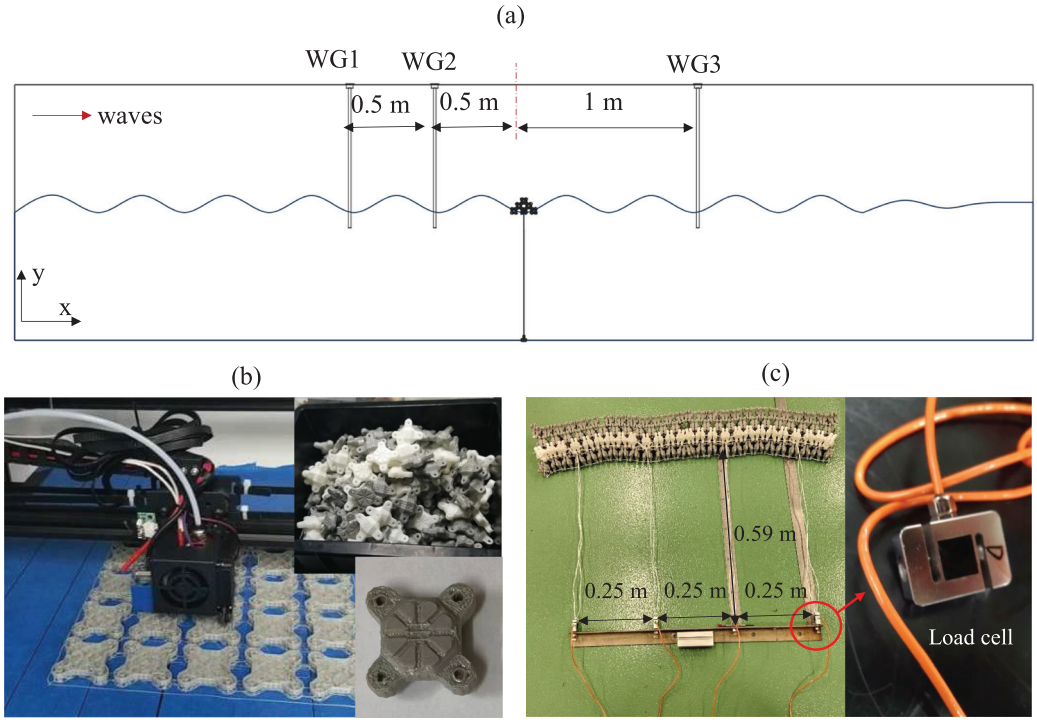

FIG. 7. The experimental setup: (a) experimental setup in the wave channel, (b) manufacturing of scaled FBs through 3D printing, and (c) pictures of the FB model and load cell.

$$\frac{\partial \rho}{\partial t} + \nabla \cdot (\rho \bar{\mathbf{u}}) = 0, \tag{3a}$$

$$\frac{\partial (\rho \bar{\mathbf{u}})}{\partial t} + \nabla \cdot (\rho \bar{\mathbf{u}} \bar{\mathbf{u}}) - \mu \nabla \cdot \nabla \bar{\mathbf{u}} - \nabla \cdot \boldsymbol{\tau}_{\mathbf{sgs}} = \nabla \bar{\mathbf{u}} \cdot \nabla \mu - \nabla p_{rgh} + \mathbf{gh} \nabla \rho + \sigma \kappa \nabla \alpha + f_{FB}. \tag{3b}$$

The SGS stress tensor is expressed in the form

$$\boldsymbol{\tau}_{sgs} = \overline{u_i u_j} - \bar{u}_i \bar{u}_j.$$

The solution scheme will be discussed in Sec. V A. Employing the Boussinesq eddy viscosity hypothesis, the SGS stress tensor is described by Eq. (4), where δ_{ij} is the Kronecker delta.[61] The isotropic part of the SGS stresses, τ_{kk}, is not modeled but is incorporated in the pressure term. Eddy viscosity SGS model using a modeled balance equation [Eq. (5)] is invoked to simulate the behavior of SGS turbulent kinetic energy (TKE) k_{sgs} (Ref. 62).

The SGS eddy viscosity, ν_{sgs}, is then calculated using the resolved scales [Eq. (6)],

$$\boldsymbol{\tau}_{sgs} = \nu_{sgs} \left(\frac{\partial \bar{u}_i}{\partial x_j} + \frac{\partial \bar{u}_j}{\partial x_i} \right) + \frac{1}{3} \delta_{ij} \tau_{kk}, \tag{4}$$

$$k_{sgs} = \frac{1}{2} \tau_{kk} = \frac{1}{2} (\overline{u_k^2} - \bar{u}_k^2),$$

$$\frac{\partial k_{sgs}}{\partial t} + \bar{u}_j \frac{\partial k_{sgs}}{\partial x_j} = -\tau_{sgs} \frac{\partial \bar{u}_i}{\partial x_j} - C_e \frac{k_{sgs}^{3/2}}{\Delta_f} + \frac{\partial}{\partial x_j} \left(\nu_{sgs} \frac{\partial k_{sgs}}{\partial x_j} \right), \tag{5}$$

$$\nu_{sgs} = C_k k_{sgs}^{1/2} \Delta_f. \tag{6}$$

where $\Delta_f = 2 \times (V_{cell})^{1/3}$ is the filter size, and C_k and C_ε are dynamically determined using the method presented in earlier works in the literature.[63]

C. Numerical schemes

The numerical study on the motions of waves and FB is conducted by using OpenFOAM, an open-source software for computational fluid dynamics. The numerical model is developed based on the existing solver, interFoam.[44] The relaxation zone method is adopted for eliminating the effects of the reflected wave.[42] The time traces of the velocity and phase fraction at the inlet boundary are pre-set using the waveVelocity and waveAlpha models. The fluid variables at the outlet are set to fixed values. Two side-planes of the NWT are treated as symmetric BCs. The top boundary in the y-direction is open to the atmosphere, and the bottom boundary is governed by a no-slip wall BC. The boundary of the FB is a moving BC, where all variables are calculated using a 6DoF solver.

The PIMPLE algorithm, a combination of PISO (Pressure Implicit with Splitting of Operator) and SIMPLE (Semi-Implicit Method for Pressure-Linked Equations) methods, is applied as the fluid solver. This could facilitate the transient solutions at higher Courant numbers.[44] For the purpose of convergence and numerical stability, the PIMPLE and PISO iteration numbers are set to be 5 and 3, respectively. The gradient and Laplacian terms of the filtered Navier–Stokes (N-S) equations are discretized utilizing the second-order-accurate Gauss linear scheme. The divergence terms are discretized by the Gauss linear upwind scheme. The second-order-accurate Crank–Nicolson scheme is used for the time derivative terms, with an

off-centering coefficient of 0.9. The equations of velocity u and SGS TKE k_{sgs} are solved utilizing smoothSolver with asymmetric Gauss–Seidel smoother. The pressure terms p and p_{rgh} are handled by the GAMG (Generalized geometric-algebraic multi-grid) solver. A semi-implicit version of the multi-dimensional limiter for explicit solution (MULES) is applied to the transport equation of the phase fraction [Eq. (2)]. It maintains the boundedness and stability of the solver at an arbitrary large Courant number.[44,50] We set the maximum number of MULES iterations over the limiter to five.

All transient simulation cases adopt adjustable time steps that conform to the Courant–Friedrichs–Lewy (CFL) condition. To avoid stability and accuracy problems due to large cell volume changes between iterations caused by a dynamic mesh, a small time step should be chosen. The solution tolerances of SGS TKE k_{sgs} and velocity u are set to be 10^{-5}. A tolerance of $10^{-6}/10^{-8}$ is employed for the pressure p/volume fraction α, respectively. The maximum Courant number of the computational domain varies according to the period of the tested wave. The maximum Courant number of the phase fraction equation, maxAlphaCo, is set to be smaller than the maximum Courant number of the N-S equations.

IV. EXPERIMENTAL SETUP

To verify the predictions of these numerical simulations, the wave attenuation performance of this FB is also measured experimentally [Fig. 7(a)]. As a full analysis of the laboratory data will be reported in a future publication, only a brief sketch of the experimental procedure will be described here. Experiments are performed in the Hydraulics Laboratory of the Hong Kong Polytechnic University. The dimensions of the irregular wave channel are 27 m in length, 1.5 m in width, and 1.5 m in height. Only regular waves are investigated in this project. The water depth is 0.6 m.

The FB components are fabricated by a 3D printer [Fig. 7(b)] and assembled through tight wires. The laboratory-scaled model is 1 m long and consists of 25 base units. The assembled FB model is then mounted to a steel angle through four wires, which are evenly spaced at 0.25 m apart. The length of each mooring wire is 0.59 m. The steel angle is then installed on the bottom of the wave tank. Three sets of wave gauges and four sets of load cells are used for the measurement of wave height and mooring forces. The weight of the load cells far exceeds the weight of the mooring wires. To minimize the effects of the load cells on the mooring system, they are installed directly on the steel angle, as the anchor points of the mooring wires [Fig. 7(c)].

The experimental results generally confirm the trends obtained computationally, with precise details to be given in a subsequent publication. A noteworthy point is the potential for applying FB as a coastal defense mechanism against storm surge during severe weather. A single FB alone cannot compete with oceanic swell generated by a typhoon/hurricane. However, suitable arrangements of multiple FBs with appropriate spacing can offer a certain degree of protection against a range of wavenumbers in the long wave regime.

V. RESULTS AND ANALYSES

A. Case study

The performance of the FBs varies with the incoming wavelength. A non-dimensional parameter, B/L_w, is introduced to formulate the relation between wave attenuation capacity and wavelength, where B is the width of the FB in the wave propagation direction and L_w is the wavelength. We shall identify a few non-dimensional parameters to gain insight into the wave dynamics. The water depth (D) is 0.6 m. Hence, a "long wave parameter" $= D/L_w$ varies from 1.54 to 0.24, and thus, we are studying waves mostly in transitional water depth regime.[64] "Wave steepness" is defined as the ratio of wave height (distance from peak to trough), H_w, to wavelength L_w. It is a measure of wave nonlinearity. The FB performance (wave attenuation), motions, and mooring force are studied in terms of these dimensionless parameters. The data collected are divided into four groups, A, B, C, and D (Table I). The first two groups describe the changes in FB performance and mooring system with the parameter B/L_w. One group (A) displays constant steepness but various wave heights, and the other one (B) includes constant wave height but varying steepness. Groups C and D concentrate on the effect of wave nonlinearity for two specific wave periods, 0.67 and 0.89 s.

In the experimental study, the test duration is 30 s for each of these test runs, and the data acquisition frequencies of the wave gauge and load cell are 40 and 1000 Hz, respectively. All simulation cases are designed to run for a time ranging from twenty to forty wave periods. The number of grid elements of the present 3D NWT with FB ranges from 2 120 000 to 3 930 000. Computations are conducted on the HPC 2021 system of the University of Hong Kong, where eight Intel Xeon 6226R processors (each processor has 16 cores) are used. The actual computing times vary from 48 to 63 h. Table I shows the conditions tested in the laboratory and numerical experiments.

B. Validation of the numerical model

The measurements of the position, posture, and motions of the FB in a laboratory is difficult. Advanced measuring techniques,

TABLE I. List of scenarios studied in this work.

Groups	Item	Wave periods (s)	Wave height, H_w (m)	D/L_w (long wave parameter)	B/L_w (FB dimension parameter)	H_w/L_w (wave steepness)
A	1	0.5	0.016	1.54	0.4	0.04
	2	0.55	0.02	1.27	0.33	
	3	0.67	0.028	0.86	0.22	
	4	0.89	0.05	0.49	0.13	
	5	1.34	0.1	0.24	0.06	
B	2	0.5	0.02	1.27	0.33	0.04
	6	0.6		1.07	0.28	0.036
	7	0.67		0.86	0.22	0.0285
	8	0.89		0.49	0.13	0.016
	9	1.34		0.24	0.06	0.008
C	7	0.67	0.02	0.86	0.22	0.028
	3		0.028			0.04
	10		0.04			0.057
	11		0.05			0.07
D	8	0.89	0.02	0.49	0.13	0.016
	12		0.03			0.024
	13		0.04			0.0325
	4		0.05			0.04
	14		0.07			0.057

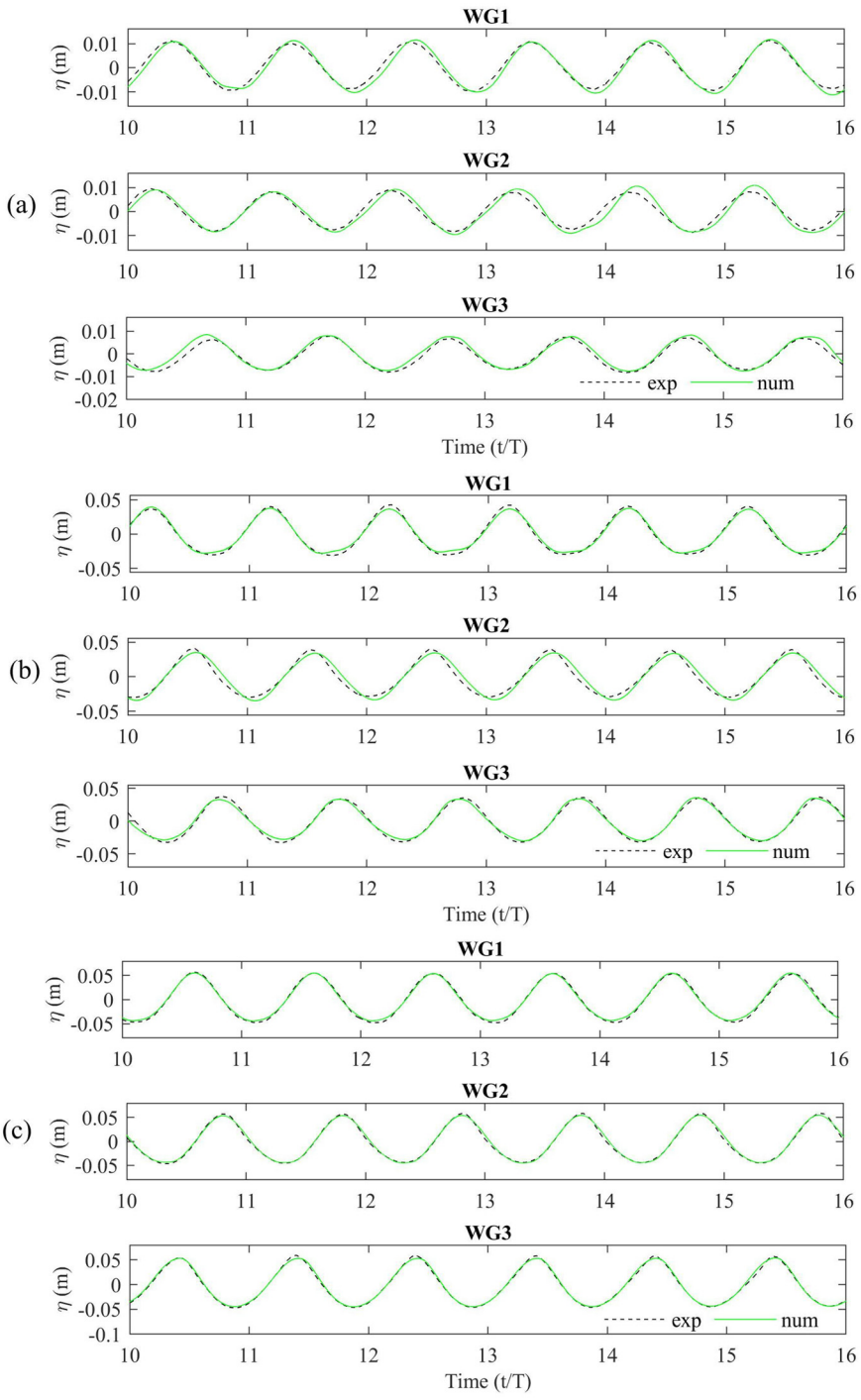

FIG. 8. Surface elevations: (a) T0.55H0.02, (b) T0.89H0.07, and (c) T1.34H0.1 (T = period, H = wave height).

e.g., high-speed particle image velocimetry (PIV) or a combination of posture sensor and accelerometer, are generally used. Here, the measurements are challenging as the FB consists of many smaller modules and the geometry is complex. The installation of sensors inside the FB and the reconstruction of FB geometry in the post-processing of PIV pictures create significant difficulties. Hence, only the wave profiles and mooring forces will be measured in the laboratory, with the goal of verifying the accuracy of the numerical model of wave–structure interaction. Numerical simulations will be performed for the same measurement conditions as the laboratory tests. The motions and

trajectories of the FB will also be tracked. Grid independence and the capacity to provide adequate resolution of the turbulent fields had been verified in our previous work.[38]

The comparisons of the numerical and experimental results of the three cases, in terms of the surface elevation and mooring force, are shown in Figs. 8 and 9. The three cases are experimental runs 2, 5, and 12, with wave periods of 0.55, 1.34, and 0.89 s, and wave heights of 0.02, 0.1, and 0.07 m, respectively. Figure 8 depicts the time traces of the surface elevation measured at three positions, in a time axis normalized by the wave period. The results show excellent agreement. The differences in data measured at wave gauge 2 (WG2) are slightly larger than the other two. WG2 represents the wave gauge closest to the FB, and is thus most heavily affected by the small perturbations caused by the motions of the FB.

A remark on the figure captions is in order. For compactness, a notation "T0.55H0.02" in Fig. 8 will denote results for a wave train with period (T) being 0.55 s and a wave height H of 0.02 m. This system of nomenclature will apply to all similar figures in this paper.

In contrast with the surface displacements, the mooring force patterns display significant changes. The laboratory FB model incorporates 25 base units and four mooring wires, while the numerical FB consists of only one base unit and two mooring lines. To compare the characteristics of experimental and numerical results, the numerical data are scaled up by a factor of 12.5 according to the simplification of the FB model. The mooring forces may have one, two, or three peaks (Fig. 9). The signals of the load cells have been preprocessed using a lowpass filter to remove noise with a frequency higher than 50 Hz, as such signal is physically impossible for the motions of FB. The mooring force of the 0.55 s period wave case still shows fluctuations at relatively high frequency (times of the incident wave frequency). The likely cause is that the mooring force is relatively small in comparison with the measuring scope of the load cell, which increases the uncertainty on the results. These computational approaches generally give very satisfactory description of wave–FB interactions (Fig. 9). Accuracy starts to degrade only for sufficiently large amplitude.

C. Analysis and comparison of results

1. Wave attenuation and energy dissipation

The measurement of the surface elevations at the front and rear portions of FB can be used to analyze the performance of the FB in terms of the transmission coefficient, reflection coefficient, and the energy dissipation rate. The transmission and reflection coefficients, K_t and K_r, respectively, correspond to the ratio of the transmitted and reflected wave height to the incident wave height, respectively. The transmission coefficient is computed using the data of WG3 and the formula below:

$$K_r = \frac{mean(H_{WG3})}{H_W}.$$

H_{WG3} stands for the wave height at wave gauge 3. The reflection coefficient is calculated through Ursell's method[65] and the data of WG1,

$$K_r = \frac{max(H_{WG1}) - min(H_{WG1})}{max(H_{WG1}) + min(H_{WG1})}.$$

Energy dissipation rate, E_{diss}, is defined to determine the amount of wave energy lost due to the viscous effect in the wave interactions and breaking caused by FB structure.

$$E_{diss} = 1 - E_r - E_t,$$

where E_r and E_t are the energy reflection and transmission rate, which are the ratio of the reflected and transmitted wave energy density to incident wave energy density, respectively. According to the linear wave theory, the energy density per unit area of gravity waves on the water surface is proportional to the wave height squared, H_i, H_r, and H_t, which are the incoming wave height, the reflected and transmitted components, respectively. The energy dissipation rate could be calculated as follows:

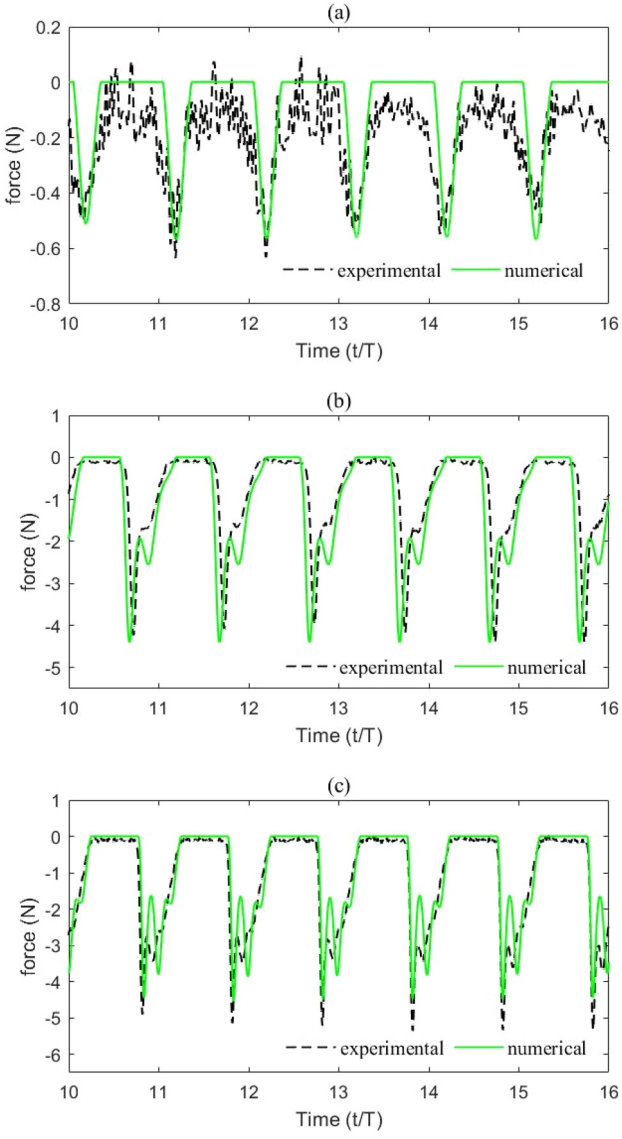

FIG. 9. Comparison of mooring forces: (a) T0.55H0.02, (b) T0.89H0.07, and (c) T1.34H0.1.

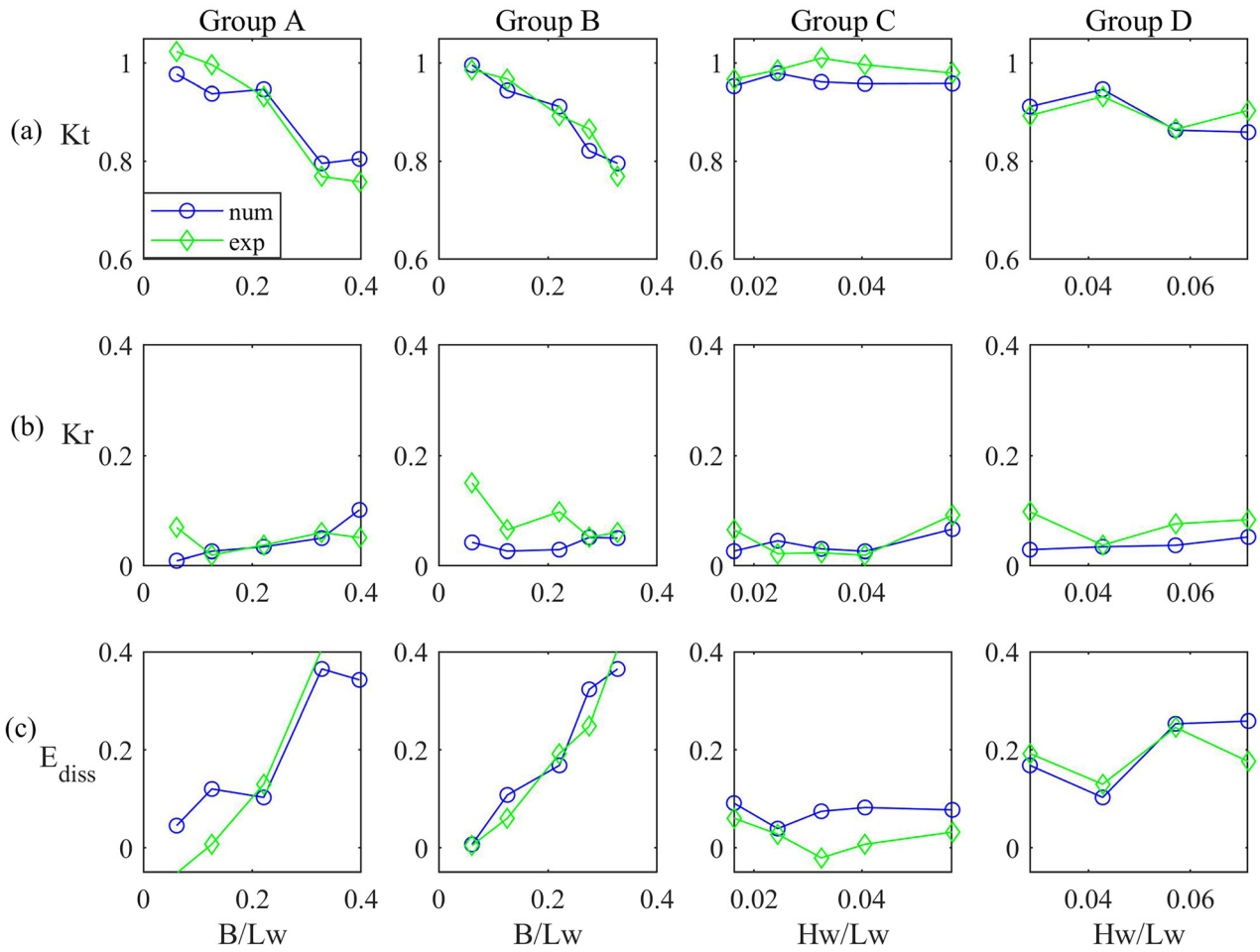

FIG. 10. Comparison of (a) transmission coefficient, (b) reflection coefficient, and (c) energy dissipation coefficient, in groups A ($H_w/L_w = 0.04$), B ($H_w = 0.02$ m), C (T = 0.89 s), and D (T = 0.67 s).

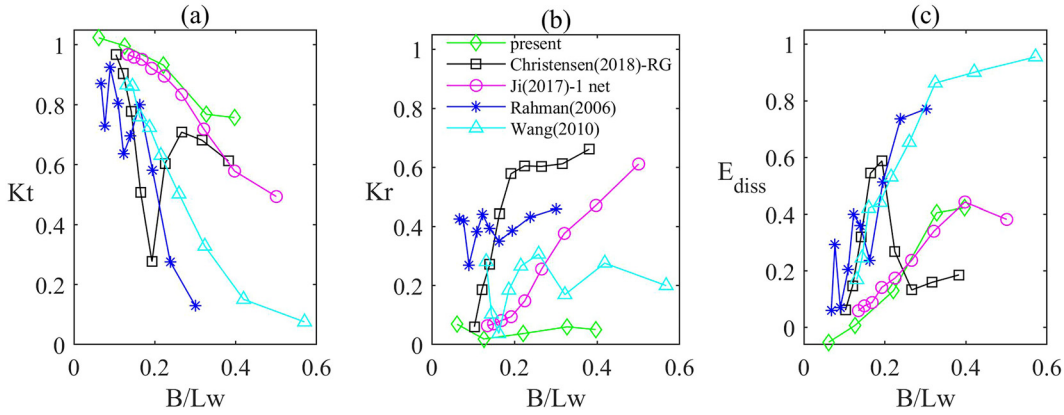

FIG. 11. Comparison of wave (a) transmission coefficient, (b) reflection coefficient, and (c) energy dissipation rate with different types of FBs.

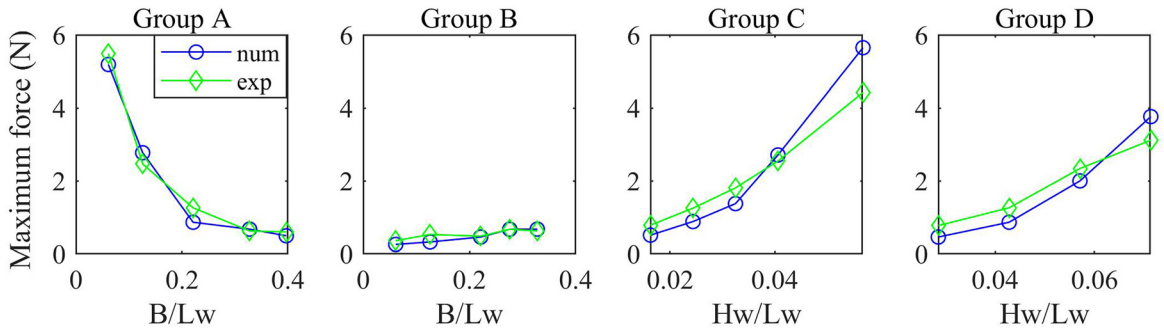

FIG. 12. Comparison of maximum mooring force, in groups A ($H_w/L_w = 0.04$), B ($H_w = 0.02$ m), C (T = 0.89 s), and D (T = 0.67 s).

$$E_{diss} = 1 - \frac{(H_t^2 + H_r^2)}{H_i^2} = 1 - K_t^2 - K_r^2.$$

Figure 10 shows the reflection (K_r) and transmission (K_t) coefficients, and dissipation energy (E_{diss}) for the four groups of tests. For situations with constant wave steepness (group A) and with identical wave height (group B), K_t decreases with larger values of B/L_w. A similar trend is observed for the transmission coefficients with increasing wave heights (groups C and D). The transmission coefficient decreases

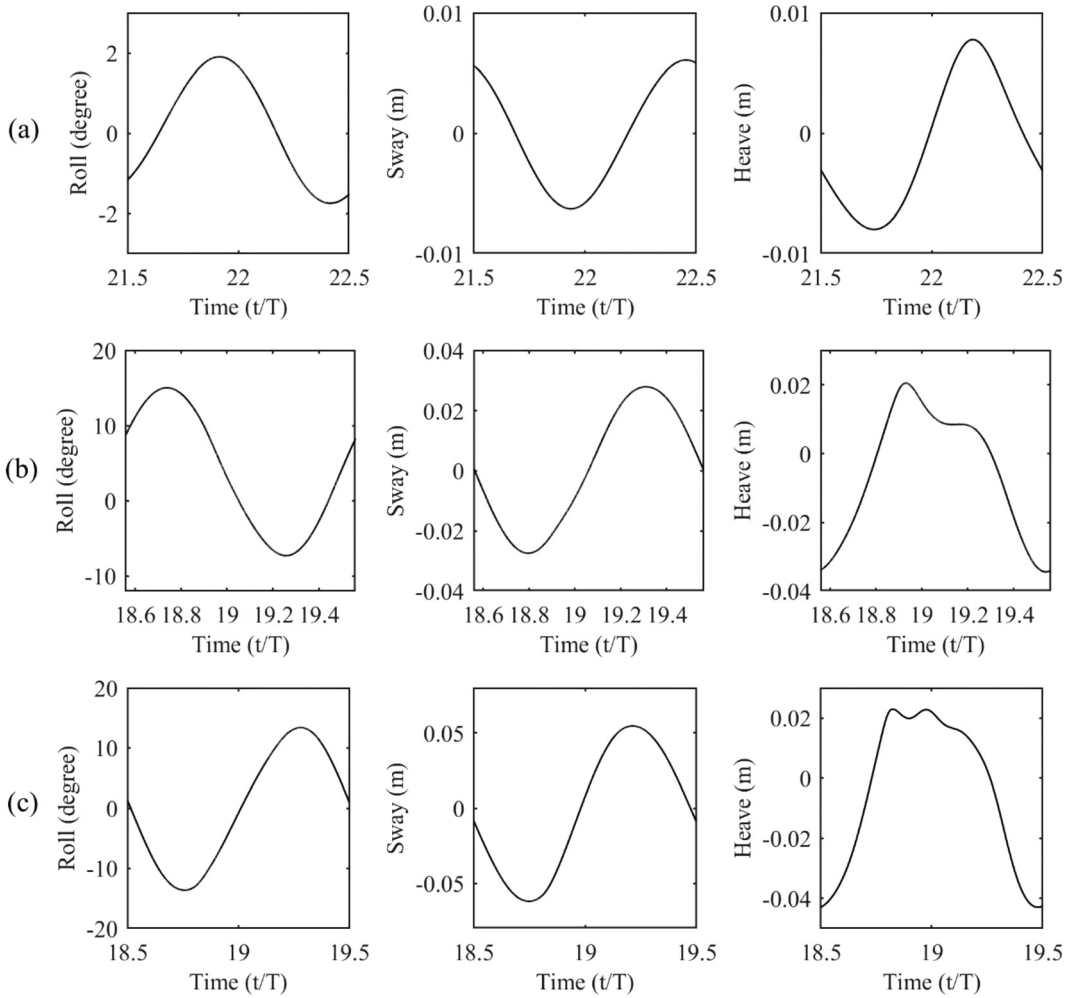

FIG. 13. Motions of FBs: (a) T0.55H0.02, (b) T0.89H0.07, and (c) T1.34H0.1.

slightly for the larger wave steepness scenarios for tests with a 0.67 s-period wave. However, K_t is over 0.9 and almost constant for all tests with a 0.89 s-period wave. For a relatively longer wave (0.89 s-period), the capacity of FB to attenuate incident waves is entirely satisfactory, even with moderate wave height.

Figure 10 also illustrates that the wave reflection coefficients of the four groups are very small, mostly less than 0.1. The reflected wave is very weak because the effective reflective area of the FB is relatively small. As shown in Fig. 2(c), the FB is porous, and the ratio of the frontal area of FB to the pore area is around 3:1. The FB surface contains symmetric segments. These features can generate further reflected waves that offset each other. When the incoming wave impinges on the FB, water will pass through the gaps and not much fluid will be reflected by the FB. This conjecture can be further verified by the contour figures of velocity and vorticity in Sec. V C 2. As the wave reflection coefficients of this FB are very small, it is reasonable to assume that the wave is attenuated mainly by the mechanism of wave dissipation [Fig. 10(c)].

As mentioned in Sec. III A, in the numerical study, the geometry of FB has been simplified, and all the fine features on surfaces designed for strengthening friction and wave breaking are eliminated to avoid mesh quality problems. The effect of this simplified geometry is not significant in the comparison of numerical and experimental results. The effects of these fine surface features on the performance of FB are probably similar in magnitude as the numerical error.

In comparison with other types of FBs,[6,8,10,26] as shown in Fig. 11, the wave attenuation performance of the studied FB is relatively weak. The porous structure of this FB may reduce the strength of the reflected wave. The slack mooring system has not provided strong constraints, which leads to little relative motions between FB and wave flow, and indeed, small energy dissipation caused by wave breaking and turbulent flow.

2. Maximum mooring force

The safety and capacity of the mooring system are also important aspects for practical applications of FB. To design or improve a mooring system that could grapple with extreme wave conditions, the maximum mooring force, a prime indicator for evaluating the strength of the mooring line, should be predicted in advance. The effects of two factors, B/L_w and wave steepness, are considered. As shown in Fig. 12, in groups A and B, two contradictory trends emerged. The maximum mooring force decreases with larger values of B/L_w for group A but increases slowly in group B. While the trends in groups C and D are consistent, the maximum mooring force increases significantly with wave steepness. Hence, the wave steepness has a small effect

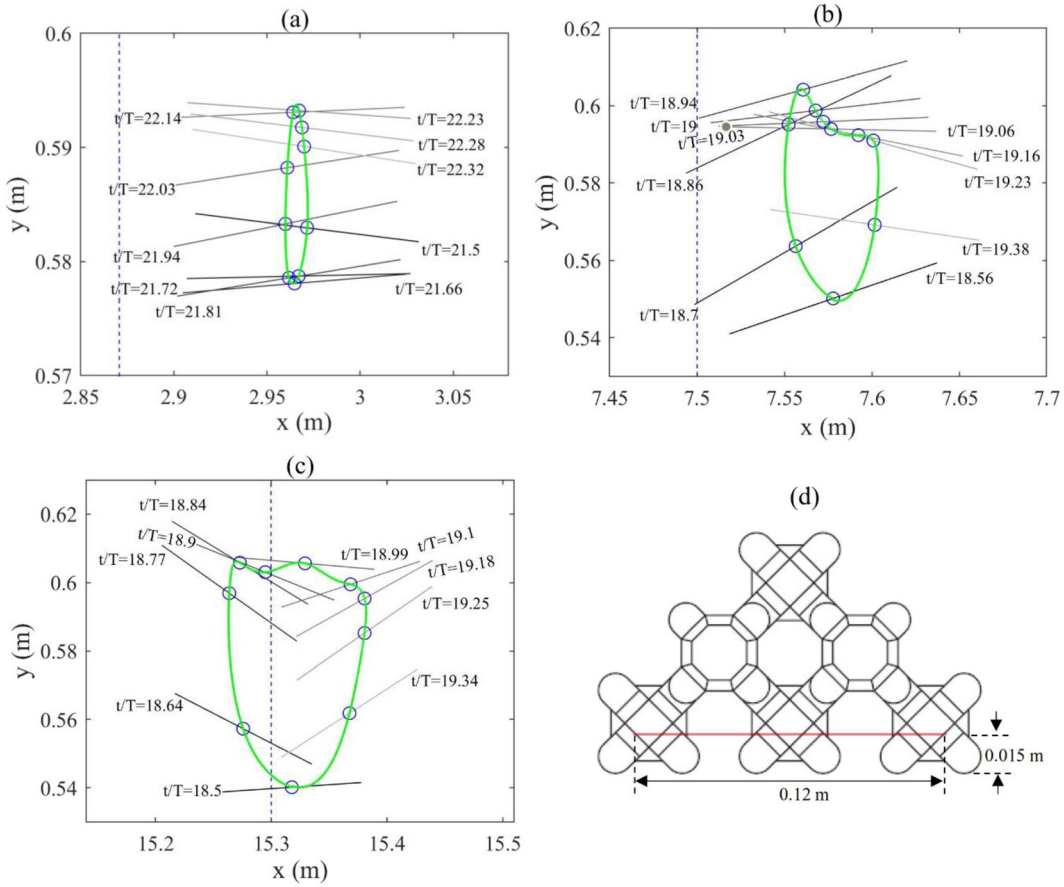

FIG. 14. Trajectories of FBs: (a) T0.55H0.02, (b) T0.89H0.07, (c) T1.34H0.1, and (d) using a straight line representing the position and orientation of FB.

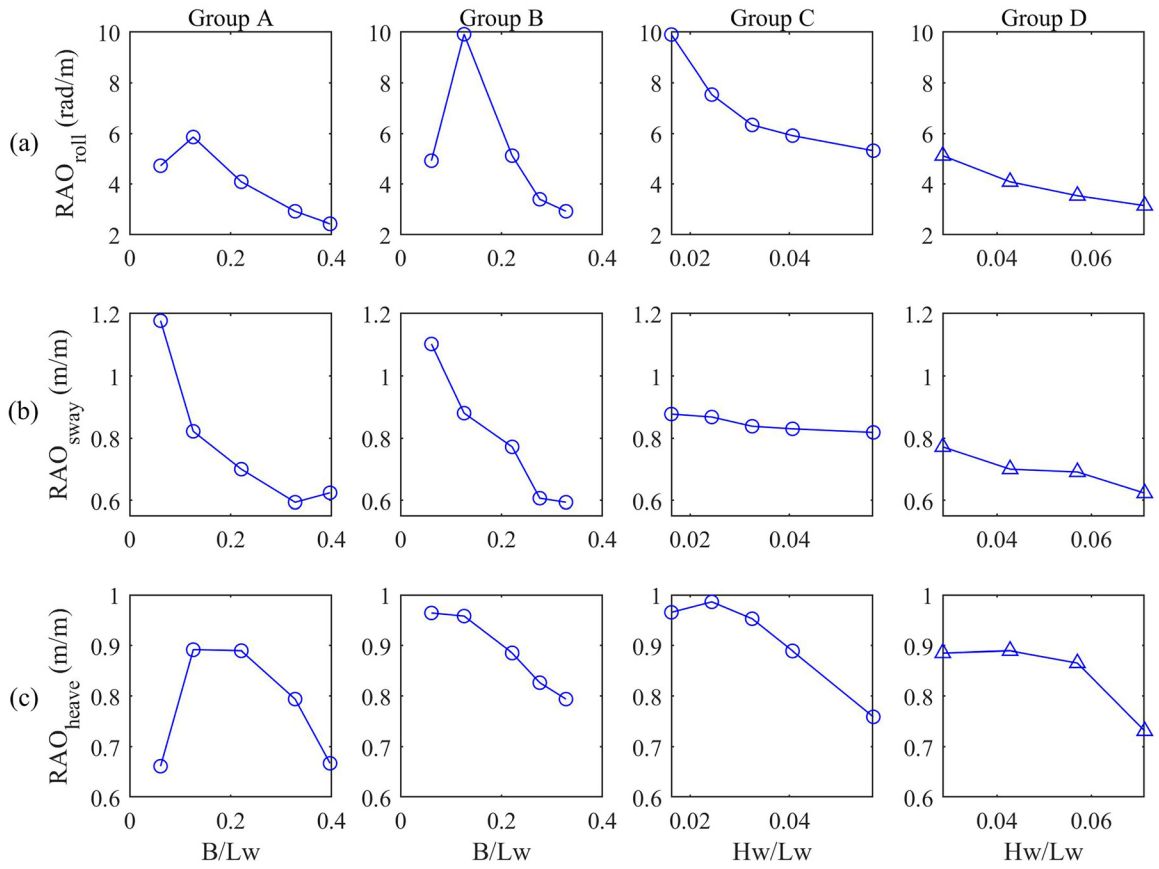

FIG. 15. Comparison of response amplitude operators (a) roll, (b) sway, and (c) heave, in groups A ($H_w/L_w = 0.04$), B ($H_w = 0.02$ m), C (T = 0.89 s), and D (T = 0.67 s).

on the wave attenuation performance of FB, but plays an important role in the motions of FB and the load of the mooring system.

3. Motions and trajectory of the floating breakwater

For a fully 3D simulation, the motions of FB in six degrees of freedom are solved. In this study, waves are monochromatic and propagate in the *x*-direction, while the structure of FB is plane-symmetric about the central plane (with a normal vector parallel to the z axis) of NWT. The translation of FB in the *z*-direction and rotations around the x and y axes are very small and are ignored. The motions of FB in the other three degrees, in general notation, roll, sway and heave, are analyzed. They are found to be directly related to

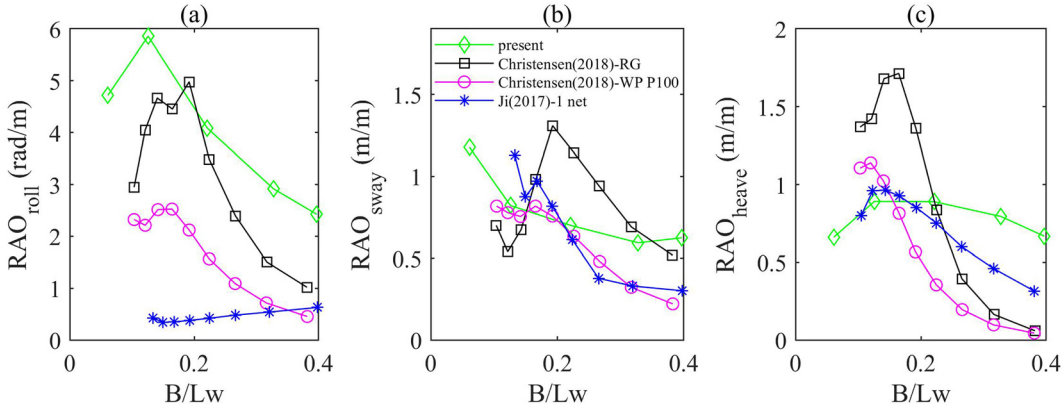

FIG. 16. Comparison of FB RAOs (a) roll, (b) sway, and (c) heave with different types of FBs.

the restraints of the mooring system and incoming wave properties. The motions of FB in three tests are shown in Fig. 13. The roll and sway motions of FB are in a sinusoidal way similar to the incident wave perturbation. Similar features hold for the heave motion for small wave height scenarios. However, if the wave height is larger than a critical level, the heave of FB shows different motion profiles, due to the constraint impacted by the tight mooring line. The time trace of heave motion echoes with the mooring force pattern in each scenario (Fig. 9), which has 1/2/3 peaks, respectively.

To express the motions of FB more directly and clearly, the trajectories of FBs in three cases are plotted in Figs. 14(a)–14(c) in a concise way. The FB is represented by a straight line [the red solid line in Fig. 14(d)]. The trajectories of the FB are illustrated using the position and orientation of the line and the trajectory of the center point of this line. The blue dash lines in Figs. 14(a)–14(c) represent the initial x axis position of FB in each scenario. There is a constant position shift of the FB in the wave propagation x-direction after a certain amount of time. This is the effect of Stokes drift. When the FB reaches the limit position, the mooring line forces the FB to move back and forth and form closed paths. The FB moves periodically with a period of the incident wave but with a different amplitude [Figs. 14(a)–14(c)]. By comparing the trajectory of FB with a free fluid element, the constraints of the mooring system on the motion of FB are shown visually.

To assess the constraints of the mooring system on the motion of the FB, the maximum displacements of FB, in the tests of four groups, are derived and analyzed (Fig. 15). The parameter, normalized response amplitude operator (RAO), is defined as the ratio of the amplitude of the FB to the amplitude of the incoming wave,

$$RAO_i = \frac{\zeta_i}{H_w/2}, \quad i = 1 - 6,$$

where RAO_i and ζ_i are the response amplitude operator and amplitude for the motion in different degrees.[8] The motions of FB are driven by wave flows and constrained by the mooring system simultaneously, which lead to complex variations of RAOs with the parameter B/L_w and wave steepness. From the results of groups C and D, the RAOs of roll and sway motions decrease with the increase in wave steepness. The RAO of heave has very gradual changes for low wave steepness scenarios, and then decreases significantly with larger values of wave steepness. A possible explanation is that both roll and sway motions are mainly controlled by the mooring line in all situations due to the Stokes drift. The heave motion of FB is not limited by the mooring system in low wave steepness tests, but is dominated by the flow-following ability of the FB.

In comparison with the RAOs of other types of FB in previous studies (Fig. 16), the values of RAOs of sway and heave motions fall within the interval of existing results, while the RAO of the roll motion is slightly higher. There are two possible reasons for the relatively larger roll motion. The inertia momentum component of this FB of this degree of freedom is smaller than other FBs, or the mooring system used in this work effects weaker restraints on this degree of freedom for the FB. This situation can be improved if one additional row of mooring lines parallel to the existing one is added.

D. Wave–FB interactions

Based on the results from the analysis of wave coefficients in Sec. V C 2, we conclude that this FB attenuates waves basically by wave dissipation due to viscosity. Viscous damping occurs both during the processes of wave propagation and wave interactions. An analytical solution of viscous damping had been given earlier in the literature.[66] For propagation over a short distance, i.e., over a few wavelengths, the effect of viscous damping is not significant. However, the presence of the FB does indeed disturb the flow, and moderates the wave profile (see Fig. 17). The interactions between wave flow and FB makeup the main contribution for wave attenuation.

Compared to a mounted breakwater, the wave transmission of a floating one is higher, due to two reasons. Part of the wave energy is translated through the water flow underlying the FB, and another part of the energy is transferred through the motions of FB (FB is disturbed by the incident wave from one side, then the motions of the breakwater cause wave radiation to the other side). The motions of the FB are constrained by the mooring system, which leads to relative motions

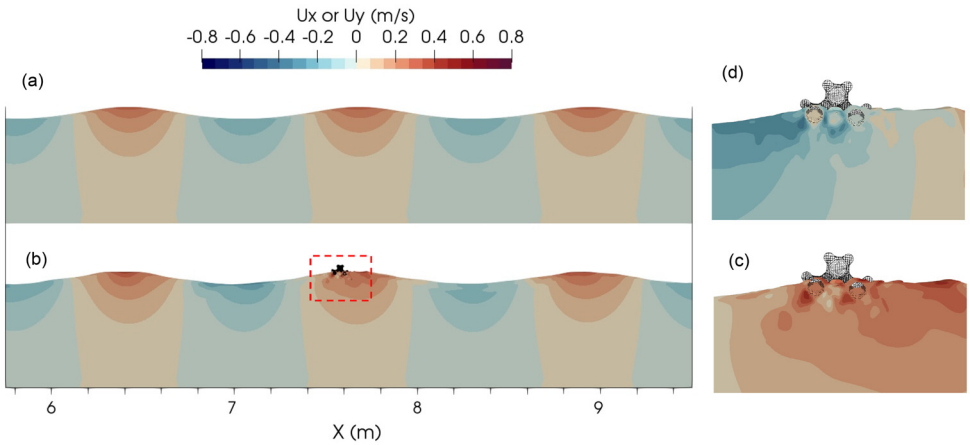

FIG. 17. Comparisons of the velocity contours of case T0.89H0.07: (a) NWT alone and (b) NWT with FB, and (c), (d) are detailed views of velocity in x (U_x) and y (U_y) direction around FB.

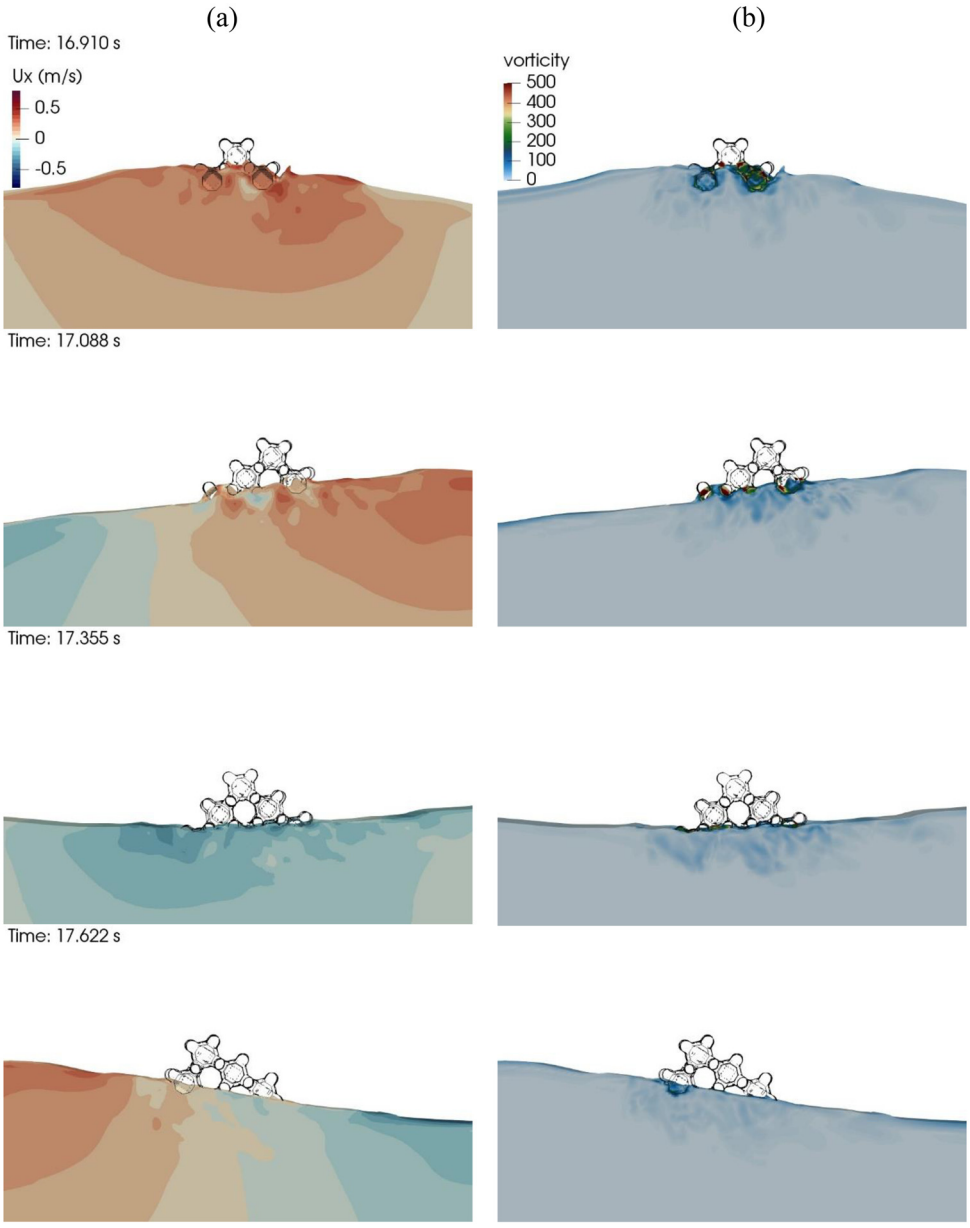

FIG. 18. Contour figures of (a) velocity and (b) vorticity of the regions around the FB, T0.89H0.07, FB with mooring system.

with wave flow, and generate eddies. The eddies interact with each other, during which turbulence kinetic energy of fluid elements dissipates into internal energy, and then increases the viscous damping of the wave. Figure 18(a) shows the fluctuation of a component of velocity component, u_x, in the region around the FB. Figure 18(b) depicts the vorticity generated due to the interactions between wave flow and FB, with a color bar indicating the magnitude of vorticity.

VI. DISCUSSIONS AND CONCLUSIONS

The wave attenuation performance and motions of a type of FB (WhisprWave) are investigated numerically and experimentally. The laboratory tests are conducted in the wave channel of the Hong Kong Polytechnic University. Wave gauges and load cells are used for recording the wave properties at the back/front of the FB and mooring forces in the mooring lines. A numerical model for wave–structure interactions is developed. The computational experiments are carried out using the HPC 2021 system of the University of Hong Kong. A mooring system model was developed and validated by experimental measurements. LES turbulence modeling is implemented for the wave breaking in the neighborhood of the FB.

The variations of wave transmission, reflection coefficient, dissipation energy rate, maximum mooring force, and RAOs with B/L_w

and wave steepness are calculated and analyzed. The wave transmission coefficient can drop to less than 0.8 if the value of B/L_w is larger than 0.3, but increase over 0.95 if the B/L_w is smaller than 0.1. To effectively protect structures behind this FB from wave erosions, e.g., a 3 m wide FB is needed to attenuate waves shorter than 10 m. The performance of the FB in attenuating long wave may not be entirely satisfactory. Our results also show that wave steepness has a larger impact on the motions of the FB and the mooring system. The maximum mooring force measured in this work can be used for the design of a mooring system in practical applications.

The motions and trajectory of FB from the results of numerical experiments are analyzed and illustrated. The time traces of heave motion are consistent with the variation of mooring force. The effect of Stokes drift on the FB movement is observed by the shift of position of the FB in the wave propagation direction. The combined effect of the constraint of the mooring system and flow following ability of the FB itself is shown through the RAO of heave motion. In low wave steepness tests, the heave RAO is limited by the flow following ability of FB, while in high wave steepness ones, the RAO is constrained by the mooring system. Relative motions between wave flow and the FB generate breaking waves and complex flow structures, which can accelerate the dissipation of wave energy. Reduction of RAOs, by using a tight mooring line or weakening the flow follow ability of the FB, can then help to enhance the wave attenuation performance.

In comparison with other types of FB studied in previous papers, the performance of this FB may need improvements in the long wave regime. Different assembly methods of the base module and section structures of this kind of FB, and improved mooring systems may enhance the efficiency in wave attenuation. Nevertheless, this type of FB exhibits many merits, e.g., flexibility of the fabrication process, diversity of the assembly modes, and convenience in transporting the equipment. Various shapes (e.g., V-shaped or arc-shaped) or arrangements (e.g., symmetric configurations) of breakwaters may involve different analysis and distinct performance characteristics.[11,67] Indeed, wave scattering mechanisms are important issues in many marine applications, e.g., fishing cage systems.[68] A further study of this type of FB is, thus, well deserved.

ACKNOWLEDGMENTS

This work was partially supported by the Research Grants Council General Research Fund (No. HKU17200718E). The computations were performed using research computing facilities offered by Information Technology Services, the University of Hong Kong. Partial financial support was provided by the Drainage Services Department of the Hong Kong Government.

AUTHOR DECLARATIONS

Conflict of Interest

The authors have no conflicts to disclose.

Author Contributions

Ning Ning Peng: Conceptualization (equal); Data curation (equal); Methodology (equal); Software (equal); Validation (equal); Writing – original draft (equal); Writing – review & editing (equal). **Wing Kin Lau:** Data curation (equal); Investigation (equal); Writing – review & editing (equal). **Wing-Hong Onyx WAI:** Conceptualization (equal); Methodology (equal); Writing – review & editing (equal). **Kwok Wing Chow:** Conceptualization (equal); Funding acquisition (equal); Methodology (equal); Supervision (equal); Writing – review & editing (equal).

DATA AVAILABILITY

The data that support the findings of this study are available from the corresponding author upon reasonable request.

REFERENCES

[1]J. Dai, C. M. Wang, T. Utsunomiya, and W. Duan, "Review of recent research and developments on floating breakwaters," Ocean Eng. **158**, 132–151 (2018).
[2]B. L. McCartney and ASCE, "Floating breakwater design," J. Waterway, Port, Coastal Ocean Eng. **111**, 304–318 (1985).
[3]T. Sawaragi, *Coastal Engineering - Waves, Beaches, Wave-Structure Interactions* (Elsevier, 1995), Vol. 78, pp. 211–270.
[4]E. Peña, J. Ferreras, and F. Sanchez-Tembleque, "Experimental study on wave transmission coefficient, mooring lines and module connector forces with different designs of floating breakwaters," Ocean Eng. **38**, 1150–1160 (2011).
[5]C. Y. Ji, X. Chen, J. Cui, Z. M. Yuan, and A. Incecik, "Experimental study of a new type of floating breakwater," Ocean Eng. **105**, 295–303 (2015).
[6]C. Ji, Y. Cheng, K. Yang, and G. Oleg, "Numerical and experimental investigation of hydrodynamic performance of a cylindrical dual pontoon-net floating breakwater," Coastal Eng. **129**, 1–16 (2017).
[7]C. Y. Ji, R. S. Zheng, J. Cui, and Z. L. Wang, "Experimental evaluation of wave transmission and dynamics of double-row floating breakwaters," J. Waterway, Port, Coastal Ocean Eng. **145**, 1–10 (2019).
[8]E. D. Christensen, H. B. Bingham, A. P. Skou Friis, A. K. Larsen, and K. L. Jensen, "An experimental and numerical study of floating breakwaters," Coastal Eng. **137**, 43–58 (2018).
[9]J. Zhan, X. Chen, Y. Gong, and W. Hu, "Numerical investigation of the interaction between an inverse T-type fixed/floating breakwater and regular/irregular waves," Ocean Eng. **137**, 110–119 (2017).
[10]H. Y. Wang and Z. C. Sun, "Experimental study of a porous floating breakwater," Ocean Eng. **37**, 520–527 (2010).
[11]Z. Zhai, X. Li, and L. Yang, "Analytical approach to the solution of short-crested wave interaction with V-shaped and arc-shaped breakwaters," Phys. Fluids **34**, 022112 (2022).
[12]N. Drimer, Y. Agnon, and M. Stiassnie, "A simplified analytical model for a floating breakwater in water of finite depth," Appl. Ocean Res. **14**, 33–41 (1992).
[13]H. Chen, R. P. Gilbert, and P. Guyenne, "Dispersion and attenuation in a porous viscoelastic model for gravity waves on an ice-covered ocean," Eur. J. Mech. B **78**, 88–105 (2019).
[14]M. Clavero, S. Longo, L. Chiapponi, and M. A. Losada, "3D flow measurements in regular breaking waves past a fixed submerged bar on an impermeable plane slope," J. Fluid Mech. **802**, 490–527 (2016).
[15]Q. Wang, H. Liu, Y. Fang, and F. Dias, "Experimental study on free-surface deformation and forces on a finite submerged plate induced by a solitary wave," Phys. Fluids **32**, 086601 (2020).
[16]J. Wang, S. Wang, X. Chen, W. Wang, and Y. Xu, "Three-dimensional evolution of internal waves reflected from a submarine seamount," Phys. Fluids **29**, 106601 (2017).
[17]R. W. Bos and P. R. Wellens, "Fluid structure interaction between a pendulum and focused breaking waves," Phys. Fluids **33**, 062118 (2021).
[18]S. M. Formentin, M. G. Gaeta, R. De Vecchis, M. Guerrero, and B. Zanuttigh, "Image-clustering analysis of the wave-structure interaction processes under breaking and non-breaking waves," Phys. Fluids **33**, 105121 (2021).
[19]G. Hou, J. Wang, and A. Layton, "Numerical methods for fluid-structure interaction—A review," Commun. Comput. Phys. **12**, 337–377 (2012).
[20]L. Huang, Y. Li, B.-M. Daniela, W. W. Christian, F. Anna, T. Sasan, D. Josh, P. Ruben, Q. Tadea, R. Edward, C. Marco, M. Li, C. Philip, and T. Gavin, "A

review on the modelling of wave-structure interactions based on OpenFOAM," OpenFOAM J. **2**, 81–93 (2022).
[21]C. Ai, Y. Ma, C. Yuan, Z. Xie, G. Dong, and T. Stoesser, "An efficient 3D non-hydrostatic model for predicting nonlinear wave interactions with fixed floating structures," Ocean Eng. **248**, 110810 (2022).
[22]S. Chen, W. Zhao, and D. Wan, "On the scattering of focused wave by a finite surface-piercing circular cylinder: A numerical investigation," Phys. Fluids **34**, 035132 (2022).
[23]R. A. Gingold and J. J. Monaghan, "Smoothed particle hydrodynamics: Theory and application to non-spherical stars," Mon. Not. R. Astron. Soc. **181**, 375–389 (1977).
[24]L. B. Lucy, "A numerical approach to the testing of the fission hypothesis," Astron. J. **82**, 1013–1024 (1977).
[25]T. Ye, D. Pan, C. Huang, and M. Liu, "Smoothed particle hydrodynamics (SPH) for complex fluid flows: Recent developments in methodology and applications," Phys. Fluids **31**, 011301 (2019).
[26]M. A. Rahman, N. Mizutani, and K. Kawasaki, "Numerical modeling of dynamic responses and mooring forces of submerged floating breakwater," Coastal Eng. **53**, 799–815 (2006).
[27]W. Peng, K. H. Lee, S. H. Shin, and N. Mizutani, "Numerical simulation of interactions between water waves and inclined-moored submerged floating breakwaters," Coastal Eng. **82**, 76–87 (2013).
[28]J. A. Sethian and S. Osher, "Fronts propagating with curvature-dependent speed: Algorithms based on Hamilton-Jacobi formulations," J. Comput. Phys. **79**, 12–49 (1987).
[29]C. Hirt and B. Nichols, "Volume of fluid (VOF) method for the dynamics of free boundaries," J. Comput. Phys. **42**, 357–366 (1981).
[30]A. J. Dunbar, B. A. Craven, and E. G. Paterson, "Development and validation of a tightly coupled CFD/6-DOF solver for simulating floating offshore wind turbine platforms," Ocean Eng. **110**, 98–105 (2015).
[31]A. Christou, T. Stoesser, and Z. Xie, "A large-eddy-simulation-based numerical wave tank for three-dimensional wave-structure interaction," Comput. Fluids **231**, 105179 (2021).
[32]R. J. McSherry, K. V. Chua, and T. Stoesser, "Large eddy simulation of free-surface flows," J. Hydrodyn. **29**, 1–12 (2017).
[33]Z. Zhou, T.-J. Hsu, D. Cox, and X. Liu, "Large-eddy simulation of wave-breaking induced turbulent coherent structures and suspended sediment transport on a barred beach," J. Geophys. Res. **122**, 207–235, https://doi.org/10.1002/2016JC011884 (2017).
[34]E. D. Christensen, "Large eddy simulation of spilling and plunging breakers," Coastal Eng. **53**, 463–485 (2006).
[35]M. Derakhti and J. T. Kirby, "Bubble entrainment and liquid-bubble interaction under unsteady breaking waves," J. Fluid Mech. **761**, 464–506 (2014).
[36]G. Ma, F. Shi, and J. T. Kirby, "A polydisperse two-fluid model for surf zone bubble simulation," J. Geophys. Res. **116**, 1–21, https://doi.org/10.1029/2010JC006667 (2011).
[37]Y. Hu, C. Liu, C. Hu, and D. Wan, "Numerical investigation of flow structure and air entrainment of breaking bow wave generated by a rectangular plate," Phys. Fluids **33**, 122113 (2021).
[38]N. N. Peng and K. W. Chow, "A numerical wave tank with large eddy simulation for wave breaking," Ocean Eng. **266**, 112555 (2022).
[39]A. Elhanafi, G. Macfarlane, A. Fleming, and Z. Leong, "Experimental and numerical investigations on the hydrodynamic performance of a floating–moored oscillating water column wave energy converter," Appl. Energy **205**, 369–390 (2017).
[40]J. Choi and S. B. Yoon, "Numerical simulations using momentum source wave-maker applied to RANS equation model," Coastal Eng. **56**, 1043–1060 (2009).
[41]P. Robinson, V. Vuko, A.-M. Moustafa, and J. Hrvoje, "Optimizing wave-generation and wave-damping in 3D-flow simulations with implicit relaxation-zones," Coastal Eng. **171**, 104035 (2021).
[42]N. G. Jacobsen, D. R. Fuhrman, and J. Fredsøe, "A wave generation toolbox for the open-source CFD library: OpenFoam," Int. J. Numer. Methods Fluids **65**, 236–253 (2011).
[43]H. Rusche, "Computational fluid dynamics of dispersed two-phase flows at high phase fractions," Ph.D. thesis (Imperial College of Science, 2002).
[44]OpenFOAM Foundation, *OpenFoam v9 User Guide* (OpenFOAM Foundation, 2021).
[45]M. Perlin and W. W. Schultz, "Capillary effects on surface waves," Annu. Rev. Fluid Mech. **32**, 241–274 (2000).
[46]D. Stagonas, D. Warbrick, G. Muller, and D. Magagna, "Surface tension effects on energy dissipation by small scale, experimental breaking waves," Coastal Eng. **58**, 826–836 (2011).
[47]J. U. Brackbill, D. B. Kothe, and C. Zemach, "A continuum method for modeling surface tension," J. Comput. Phys. **100**, 335–354 (1992).
[48]V. T. Nguyen and W. G. Park, "A volume-of-fluid (VOF) interface-sharpening method for two-phase incompressible flows," Comput. Fluids **152**, 104–119 (2017).
[49]V. Maltsev, M. Skote, and P. Tsoutsanis, "High-order methods for diffuse-interface models in compressible multi-medium flows: A review," Phys. Fluids **34**, 021301 (2022).
[50]OpenFOAM Foundation, *Interface Capturing in OpenFOAM* (OpenFOAM Foundation, 2020).
[51]J. Roenby, H. Bredmose, and H. Jasak, "A computational method for sharp interface advection," R. Soc. Open Sci. **3**, 160405 (2016).
[52]W. J. Rider and D. B. Kothe, "Reconstructing volume tracking," J. Comput. Phys. **141**, 112–152 (1998).
[53]D. Bi, T. Sun, Y. Wei, and X. Huang, "On the dynamic behaviors of freely falling annular disks at different Reynolds numbers," Phys. Fluids **34**, 043307 (2022).
[54]F. Depalo, S. Wang, S. Xu, C. Guedes Soares, S.-H. Yang, and J. W. Ringsberg, "Effects of dynamic axial stiffness of elastic moorings for a wave energy converter," Ocean Eng. **251**, 111132 (2022).
[55]H. D. Pham, P. Cartraud, F. Schoefs, T. Soulard, and C. Berhault, "Dynamic modeling of nylon mooring lines for a floating wind turbine," Appl. Ocean Res. **87**, 1–8 (2019).
[56]J. D. Fenton, "A fifth-order Stokes theory for steady waves," J. Waterway, Port, Coastal, Ocean Eng. **111**, 216–234 (1985).
[57]D. R. Fuhrman, P. A. Madsen, and H. B. Bingham, "Numerical simulation of lowest-order short-crested wave instabilities," J. Fluid Mech. **563**, 415–441 (2006).
[58]S. Seng, "Slamming and whipping of ships," Ph.D. thesis (Technical University of Denmark, 2012).
[59]J. Hrvoje and T. Zeljko, "Dynamic mesh handling in OpenFOAM applied to fluid-structure interaction simulations," in *Proceedings of the V European Conference on Computational Fluid Dynamics* (ECCOMAS, 2010), pp. 1–19.
[60]J. W. Deardorff, "A numerical study of three-dimensional turbulent channel flow at large Reynolds numbers," J. Fluid Mech. **41**, 453–480 (1970).
[61]J. O. Hinze, *Turbulence* (McGraw-Hill Publishing Co., New York, 1975).
[62]U. Schumann, "Subgrid scale model for finite difference simulations of turbulent flows in plane channels and annuli," J. Comput. Phys. **18**, 376–404 (1975).
[63]W.-W. Kim and S. Menon, "A new dynamic one-equation subgrid-scale model for large eddy simulations," in Proceeding of 33rd Aerospace Sciences Meeting and Exhibit (1995).
[64]R. Dean and R. Dalrymple, *Water Wave Mechanics for Engineers and Scientists*, Advanced Series on Ocean Engineering Vol. 2 (World Scientific Publishing, 1991).
[65]F. Ursell, R. G. Dean, and Y. S. Yu, "Forced small-amplitude water waves: A comparison of theory and experiment," J. Fluid Mech. **7**, 33–52 (1960).
[66]C. C. Mei, *Theory and Applications of Ocean Surface Waves* (World Scientific Publishing, Singapore, 2005).
[67]H. S. Zhang, P. X. Zhou, and G. W. Hong, "Mathematical model of wave diffraction for symmetrically arranged breakwaters," Phys. Fluids **34**, 067102 (2022).
[68]S. A. Selvan, R. Gayathri, H. Behera, and M. H. Meylan, "Surface wave scattering by multiple flexible fishing cage system," Phys. Fluids **33**, 037119 (2021).